

**UNIVERSIDADE FEDERAL DE SÃO CARLOS  
CENTRO DE CIÊNCIAS EXATAS E DE TECNOLOGIA  
PROGRAMA DE PÓS-GRADUAÇÃO EM CIÊNCIA E  
ENGENHARIA DE MATERIAIS**

PROCESS PARAMETERS OPTIMIZATION AND MICROSTRUCTURE  
EVALUATION ON FRICTION SPOT-WELDED ALUMINUM/COPPER  
DISSIMILAR JOINTS

Maria Eduarda Barbosa Cardillo

São Carlos  
2016



**UNIVERSIDADE FEDERAL DE SÃO CARLOS  
CENTRO DE CIÊNCIAS EXATAS E DE TECNOLOGIA  
PROGRAMA DE PÓS-GRADUAÇÃO EM CIÊNCIA E  
ENGENHARIA DE MATERIAIS**

**PROCESS PARAMETERS OPTIMIZATION AND MICROSTRUCTURE  
EVALUATION ON FRICTION SPOT-WELDED ALUMINUM/COPPER  
DISSIMILAR JOINTS**

Maria Eduarda Barbosa Cardillo

Dissertation presented to  
Programa de Pós-Graduação em Ciência e  
Engenharia de Materiais to obtain the  
MASTER OF SCIENCE DEGREE IN  
MATERIALS SCIENCE AND ENGINEERING

Supervisor: Dr. Nelson Guedes de Alcântara.

Grant Agency: CAPES

São Carlos  
2016



## RESUME

Bachelor of Science in Materials Engineering (2015).



**UNIVERSIDADE FEDERAL DE SÃO CARLOS**

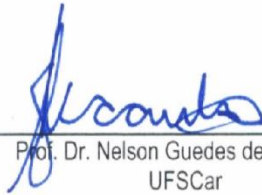
Centro de Ciências Exatas e de Tecnologia  
Programa de Pós-Graduação em Ciência e Engenharia de Materiais

---

**Folha de Aprovação**

---

Assinaturas dos membros da comissão examinadora que avaliou e aprovou a Defesa de Dissertação de Mestrado da candidata Maria Eduarda Barbosa Cardillo, realizada em 17/11/2016:



---

Prof. Dr. Nelson Guedes de Alcântara  
UFSCar



---

Prof. Dr. José Eduardo Spinelli  
UFSCar

---

Prof. Dr. Jorge Fernandez dos Santos  
WMP/HZG

Certifico que a sessão de Defesa realizou-se com a participação à distância do membro Jorge Fernandez dos Santos e, depois das arguições e deliberações realizadas, o participante à distância está de acordo com o conteúdo do Parecer da Comissão Julgadora redigido neste Relatório de Defesa.



---

Prof. Dr. Nelson Guedes de Alcântara – Presidente de Comissão Julgadora





## ACKNOWLEDGMENTS

Firstly, I would like to express my gratitude to Dr. Junjun Shen, my scientific advisor at the Helmholtz-Zentrum Geesthacht, for the supportive orientation, availability and willingness to share his knowledge.

I am also grateful to Dr. Jorge dos Santos, for the work opportunity created and for the supervision and support, not only on a professional basis, but also on a personal level. Dr. Santos allowed me to grow, both professionally and personally, being it a great experience for me, to have been part of the excellent work group that he so delicately runs.

To Prof. Dr. Nelson Guedes de Alcântara, I phrase my appreciation, for the opportunity, trust, support, attention, motivation and encouragement provided during the development of my work.

I also received invaluable help from friends, especially Gonçalo Cipriano, a wise and perceptive critic, who read the first draft of this work and commented from a PhD student perspective. Also Thiago Pama for his support with the *Thermocalc* Software and friendship during the course of this work.

I thank my family members, Eduardo Cardillo, Cláudia Cardillo, Roberto Cardillo and Lucas Cardillo, for their love and patience. I cannot find enough words to thank them for all they have done for me.

For those friends that became family, Isabela Loiola, Janaína Kawasaki, Larissa Dias, Rafael Halfed, Murillo Romero, Stella Risso and Thaísa Lemos, although we all take different paths in life, no matter where we go, we take a little bit of each other anywhere.

Finally, to everyone that although not mentioned here by name have at some point and somehow contributed to my academic path.



## ABSTRACT

Dissimilar materials welding is a field of increasing interest for a wide range of industrial applications. Specifically, the welding of aluminum alloys with copper has potential applications in the heating, ventilation and air conditioning (HVAC) industries, being used for the production of electrical and thermal connections. However, these applications require the development of reliable, efficient and economic welding processes. Mismatches between the material's physical properties and metallurgical factors make the identification of an adequate welding process and parameters a challenge to be overcome. In the present research work, friction spot welding (FSpW) was applied to create welded joints between AA5083-O and phosphorus-deoxidized copper. The objectives were: to optimize the process parameters and to determine the dominant factors by means of design of experiments; to comprehend the microstructure formation mechanism; and to determine the fracture behaviors of the welds under shear loading. For these purposes, mechanical testing and metallographic analyses were used to evaluate the welded joints. Lap-shear strength was chosen to determine the weld quality and microhardness tests were done in order to better understand the specific local mechanical resistance of the different welding zones. Microstructural analyses were performed by means of optical microscopy, scanning electron microscopy, energy dispersive spectroscopy and by the electron backscatter diffraction technique. The software *Thermocalc* was also used to theorize the intermetallic formation. The results confirmed the effectiveness of the FSpW technique when applied to weld the dissimilar metals Al and Cu. The plunge depth welding parameter was determined statistically as the dominant factor in Al and Cu friction spot-welded joints. Mainly, due to its effect on the formation of a deformed metallic volume just below the interface. Microscopically, two intermetallic compounds were identified across the interface and micro-constituents with characteristics of an eutectic structure were also observed in some welding conditions. This metallurgical feature is detrimental to the mechanical properties, and therefore must be controlled.

**Keywords:** Friction Spot Welding; Aluminum; Copper.



## RESUMO

A soldagem de alumínio e cobre tem grande potencial de aplicação no setor HVAC (*heating, ventilation and air conditioning*), podendo ser usada para a fabricação de trocadores de calor e circuitos elétricos mais leves e baratos. Para isso, uma tecnologia de soldagem confiável, eficiente e econômica deve ser utilizada. No entanto, as diferentes propriedades físicas dos materiais e problemas metalúrgicos tornam a identificação da técnica e dos parâmetros de soldagem, um desafio a ser superado. Neste trabalho, o processo de soldagem por fricção por ponto (FSpW) foi aplicado para criar uniões entre a liga de alumínio 5083-O e cobre desoxidado com fósforo. Os objetivos definidos foram: otimizar os parâmetros do processo em função do desempenho mecânico da junta soldada; analisar os mecanismos de formação microestrutural; e compreender os comportamentos de fratura das soldas submetidas a um esforço de cisalhamento. Para estes propósitos, as soldas foram avaliadas através de ensaios mecânicos e análises metalográficas. O ensaio de cisalhamento foi escolhido como resposta para determinar a qualidade das juntas soldadas e ensaios de microdureza foram feitos com o intuito de melhor compreender as propriedades mecânicas locais das diferentes zonas de soldagem. Análises microestruturais foram feitas com o uso de microscópio ótico, microscópio eletrônico de varredura, espectrômetro de energia dispersiva e pela técnica de difração de elétrons retro-espalhados. O software *Thermocalc* também foi usado para melhor compreender as prováveis fases que formariam durante o processo. Os resultados comprovaram a efetividade da técnica FSpW, quando aplicada para unir os metais dissimilares Al e Cu. O parâmetro de soldagem profundidade de penetração revelou estatisticamente um efeito significativo sobre a resistência mecânica das juntas soldadas. Sobretudo, devido ao efeito deste parâmetro na formação de um volume de metal deformado na interface. Microestruturalmente, duas camadas de intermetálicos foram identificadas ao longo da interface e em certas condições de soldagem, microconstituintes resultantes de reações eutéticas foram observados. Esta característica metalúrgica é prejudicial às propriedades mecânicas das juntas soldadas e por isso deve ser controlada.

**Palavras-chave:** Friction Spot Welding; Alumínio; Cobre.



**PUBLICATION**

J. Shen, U. F. H. Suhuddin, M. E. B. Cardillo, and J. F. dos Santos, "Eutectic structures in friction spot welding joint of aluminum alloy to copper," *Applied Physics Letters*, vol. 104, no. 19, May 2014.





## TABLE OF CONTENTS

CERTIFICATE OF APPROVAL.....	i
ACKNOWLEDGMENTS.....	iii
ABSTRACT .....	v
RESUMO .....	vii
PUBLICATION .....	ix
TABLE OF CONTENTS .....	xi
TABLE LIST .....	xiii
FIGURE LIST .....	xv
SYMBOLS AND ABBREVIATIONS .....	xxi
1 MOTIVATION .....	1
2 OBJECTIVES .....	3
3 LITERATURE REVIEW .....	5
3.1 Literature Survey on the Materials .....	5
3.1.1 Al and Al Alloys.....	5
3.1.2 Cu and Cu Alloys.....	8
3.2 Review on Aluminum/Copper and Aluminum/Copper/Magnesium System.....	11
3.3 Friction Spot Welding.....	13
3.3.1 Process Description.....	13
3.3.2 Process Parameters .....	16
3.3.3 Energy Input .....	17
3.3.4 Characterization of the Welding Zones.....	19
3.3.5 Fracture Behavior under Shear Loading.....	21
3.4 Design of Experiments .....	23
4 MATERIALS AND METHODS.....	27
4.1 Joining Equipment and Procedure .....	27
4.2 Welding Parameters.....	28
4.3 Mechanical Characterization.....	29
4.3.1 Lap-shear Testing.....	29
4.3.2 Microhardness Testing .....	30

4.4	Metallurgical Characterization .....	30
4.5	Temperature Measurements .....	31
4.6	Research Methods .....	32
5	RESULTS AND DISCUSSIONS .....	35
5.1	Screening Stage .....	35
5.1.1	Influence of the Tool Geometry .....	35
5.1.2	Influence of the Clamping Force .....	37
5.1.3	Influence of the Sleeve Plunge Time and Retraction Time .....	38
5.2	Thermal Evaluation.....	39
5.2.1	Typical Welding Thermal Cycle.....	39
5.2.2	Influence of Welding Parameters on Thermal Cycle .....	40
5.3	Process Parameters Optimization .....	44
5.3.1	Individual Process Parameters .....	44
5.3.2	Interactions .....	49
5.4	Macro and Microstructural Features .....	51
5.4.1	Typical Macro and Microstructural Features .....	51
5.4.2	Microstructure Formation Mechanism .....	54
5.5	Local Mechanical Resistance .....	63
5.6	Influence of Process Parameters on Macrograph and LSS.....	64
5.7	Fracture Surface Analyses .....	67
5.7.1	Typical Fracture Behaviors .....	67
5.7.2	Plug Pullout with Tearing .....	69
6	CONCLUSIONS.....	75
7	RECOMMENDATIONS FOR FUTURE WORK.....	77
8	REFERENCES .....	79

## TABLE LIST

Table 3.1 Typical chemical composition of AA5083-O (weight %) [15]. .....	7
Table 3.2 Main mechanical, physical, thermal and electrical properties of AA5083-O at room temperature [15]. .....	8
Table 3.3 Nominal chemical composition of Cu-DHP (weight %) [19]. .....	10
Table 3.4 Main mechanical, physical, thermal and electrical properties of Cu-DHP at room temperature [19]. .....	10
Table 3.5 Composition information of the Al/Cu binary system compounds, according to Ponweiser [22]. .....	12
Table 4.1 Welding parameters variation. ....	29
Table 4.2 Grinding and polishing procedures. ....	31
Table 5.1 Influence of a threaded and non-threaded geometry on the LSS and respective fracture surface diameter. Welding condition: RS = 1500 rpm, PD = 2 mm, DT = 2 s, CF = 17.48 kN, PT = 2 s, RT = 1 s. ....	37
Table 5.2 Influence of the CF on the LSS and respective fracture surface diameter. Welding condition: RS = 1200 rpm, PD = 2 mm, DT = 2 s, PT = 2 s, RT = 1 s. ....	38
Table 5.3 Influence of the PT on the LSS and respective fracture surface diameter. Welding condition: RS = 1200 rpm, PD = 1.6 mm, DT = 1 s, RT = 1 s. ....	39
Table 5.4 Influence of DT on the welding peak temperature. Welding condition: RS = 1200rpm, PD = 1.6 mm. ....	42
Table 5.5 Influence of PD on the welding peak temperature. Welding condition: RS = 1200 rpm, DT = 2 s. ....	43
Table 5.6 Influence of RS on the welding peak temperature. Welding condition: PD = 1.6 mm, DT = 0. ....	44
Table 5.7 Taguchi design of experiments, the response of each run is displayed in the rightmost column. ....	45
Table 5.8 Analysis of variance for the average LSS. ....	46
Table 5.9 One-factor-at-a-time matrix of experiments. ....	47
Table 5.10 Factors and levels for the full factorial design. ....	50

Table 5.11 Full factorial design of experiments used to evaluate the influence of the individual parameters and interactions, the response for each run is displayed in the rightmost column.....	50
Table 5.12 Elemental composition of different locations in Figure 5.35 (atomic %). .....	71
Table 5.13 Elemental composition of different locations in Figure 5.36 (atomic %). .....	72
Table 5.14 Elemental composition of different locations in Figure 5.37 (atomic %). .....	73

## FIGURE LIST

Figure 3.1 Chart with the material indexes normalized by the values of cast iron [8].	6
Figure 3.2 Al/Cu binary diagram [21].	11
Figure 3.3 Schematic illustration of the three-piece tool system used in the FSpW process [28].	14
Figure 3.4 Schematic representation of the FSpW process - sleeve penetration variant: (a) clamping and spindle rotation; (b) sleeve plunges into the upper sheet while the pin moves upward; (c) spindles retract back and (d) withdrawal of the welding head.	15
Figure 3.5 Relation between the tool rotational speed and the torque during FSSW of AA6061 and AM50 [33].	18
Figure 3.6 Weld strength as function of (a) bonded area and (b) energy input [35].	18
Figure 3.7 Weld strength and fracture modes as function of bonded area [36].	19
Figure 3.8 Cross section macrograph and hardness profile of an AA6181 friction spot-welded joint [39].	20
Figure 3.9 Optical microscope images of the distinct welding zones in AA6181 friction spot-welded joints (a) deformed grains in the TMAZ and (b) refined microstructure in the SZ [39].	20
Figure 3.10 FSSW of dissimilar AA5754/AA6111 (a) macrograph and (b) intermixed zone [42].	21
Figure 3.11 Friction spot-welded joints fracture modes in lap-shear tensile test: (a) through the interface, (b) plug pullout with tearing and (c) variants of plug pullout [39].	22
Figure 3.12 Force vs. displacement curve observed during lap-shear testing of friction spot-welded AA2024 [4].	23
Figure 4.1 RPS 100 FSpW machine used to produce Al/Cu welds [46].	28
Figure 4.2 Clamping system used to fix the sheets against the backing rod.	28
Figure 4.3 Al/Cu friction spot-welded sample for lap-shear testing.	29
Figure 4.4 Machine Zwick/Roell used for lap-shear test.	30

Figure 4.5 Schematic illustration of the thermocouple positioning, superimposed with the tool profile.....	32
Figure 4.6 Work-packages established for this work. ....	33
Figure 5.1 Bonded width measurement procedures, according to the: (a) fracture surface and (b) cross section of the welded joint. ....	35
Figure 5.2 FSpW tools used to optimize the process: (a) threaded and (b) non-threaded geometries.....	36
Figure 5.3 As-etched macrographs obtained with a (a) threaded and (b) non-threaded tool. White dashed circle in (a) indicates the deformed metallic volume under the interface. Welding condition: RS = 1200 rpm, PD = 2 mm, DT = 1 s, CF = 17.48 kN, PT = 2 s, RT = 1 s. ....	37
Figure 5.4 As-etched macrographs obtained with a CF of (a) 14.56 kN and (b) 17.48 kN. Magnified view taken from the indentation: (c) location marked with a white box in (a) and (d) location marked with a white box in (b). Welding condition: RS = 1200 rpm, PD = 2 mm, DT = 2 s, PT = 2 s, RT = 1s.....	38
Figure 5.5 As-polished macrographs obtained with a PT of (a) 1 s and (b) 2 s. Welding condition: RS = 1200 rpm, PD = 1.6 mm, DT = 1 s, RT = 1 s. ....	39
Figure 5.6 Typical thermal cycle of Al/Cu friction spot-welded joints. Welding condition: RS = 1200 rpm, PD = 1.6 mm, DT = 1 s.....	40
Figure 5.7 Temperature profile of comparative PT: 1 s and 2s. Welding condition: RS = 1200 rpm, PD = 1.6 mm, DT = 1 s.....	41
Figure 5.8 Temperature profile of comparative DT: 0, 1 s and 2 s. Welding condition: RS = 1200 rpm, PD = 1.6 mm. ....	41
Figure 5.9 Temperature profile of comparative DT: 1 s and 2 s. The serrated feature is shown in detail. Welding condition: RS = 2000 rpm, PD = 2 mm. ....	42
Figure 5.10 Temperature profile of comparative plunge depths: 1.6 mm, 1.8 mm and 2 mm. Welding condition: RS = 1200 rpm, DT = 2 s.....	43
Figure 5.11 Temperature profile of comparative rotational speeds: 1200 rpm, 1500 rpm and 2000 rpm. Welding condition: PD = 1.6 mm, DT = 0. ....	44
Figure 5.12 Normal probability plot.....	46
Figure 5.13 Effect of each level on the average LSS: (a) tool rotational speed, (b) dwell time and (c) plunge depth.....	47

Figure 5.14 LSS response according to the OFAT plan: (a) DT variation (RS = 1200 rpm and PD = 2 mm), (b) RS variation (PD = 2 mm and DT = 2 s) and (c) PD variation (RS = 1200 rpm and DT = 2 s).....	48
Figure 5.15 Interaction plots, obtained by the <i>Minitab</i> software. ....	49
Figure 5.16 Pareto plot analysis of the individual parameters and interactions.	51
Figure 5.17 Typical Al/Cu friction spot-welded joint: (a) cross section of the as-etched sample, the four white boxes indicate the region for SEM analyses in Figure 5.19; (b) back-scattered image from the as-polished sample, it was taken from the location marked with a yellow dashed box in (a). Welding condition: RS = 1200 rpm, PD = 1.6 mm, DT = 0. ....	52
Figure 5.18 Similar AA5083 friction spot-welded joint. Welding condition: RS = 1200 rpm, PD = 1.6 mm, DT = 0. ....	52
Figure 5.19 Typical microstructures of the Al/Cu welded joint: (a) weld rim, (b) BM, (c) weld center, (d) interface under the sleeve, and (e) interface at the weld center. ....	53
Figure 5.20 Fine particles observed at a RS of 2000 rpm, PD of 1.6 mm and DT of 0: (a) cross section of the welded joint, (b) magnified view taken from the location marked with a yellow box in (a), (c) magnified view taken from the location marked with a white box in (b), and EDS maps taken from (c): (d) Al and (e) Cu. ....	54
Figure 5.21 (a) Cross section of the welding condition RS = 1200 rpm, PD = 2.2 mm, DT = 2 s, the white box indicates the region for SEM analyses; (b) overview of the sleeve-plunge area, five white boxes indicate the positions of the subsequent SEM analyses; (c) and (d) swirl and vortex patterns; (e), (f) and (g) Cu fragments observed around the weld rim; (h) diffusion patterns; (i) intermetallic layers formed around each Cu fragment in the Al matrix. ....	57
Figure 5.22 Intermetallic layers observed at the weld center: (a) welding condition: RS = 1200 rpm, PD = 2.2 mm, DT = 2 s and (b) welding condition: RS = 1200, PD = 1.6, DT = 0. ....	58
Figure 5.23 Theoretical constituents that would form considering a mixture of Cu into the Al sheet of: (a) 20, (b) 25, (c) 30, (d) 35, (e) 40 and (f) 45 (weight %). ....	59

Figure 5.24 (a) Cross section; (b) region with eutectic features, taken from the location marked with a yellow box in (a); (c) details of the eutectic region, taken from the white box in (b). Welding condition: RS = 2000 rpm, PD = 2 mm, DT = 1 s.....	60
Figure 5.25 EDS maps: (a) field of view, (b) Al, (c) Cu, and (d) Mg.....	61
Figure 5.26 Isothermal section of ternary Al/Cu/Mg phase diagram at 400°C, $\theta = \text{CuAl}_2$ , $S = \text{MgCuAl}_2$ and $T = (\text{Cu}_{1-x}\text{Al}_x)_{49}\text{Mg}_{32}$ . The red star indicates the composition point: 90Al-4Cu-6Mg, which corresponds to the average composition of the eutectic region [55]. .....	62
Figure 5.27 EDS spectrums and the corresponding Kikuchi patterns of points i and ii marked in Figure 5.24 (c). .....	62
Figure 5.28 Typical hardness profile and respective cross section. Welding condition: RS = 1200 rpm, PD = 2 mm, DT = 2 s.....	64
Figure 5.29 Macrograph of comparative: dwell time levels (a) 0, (b) 1 and (c) 2 s (rotational speed of 1200 rpm and plunge depth of 1.6 mm); plunge depth levels (d) 1.6, (e) 1.8 and (f) 2 mm (rotational speed of 1200 rpm and dwell time of 2 s); rotational speed levels (g) 1200, (h) 1500 and (i) 2000 rpm (plunge depth of 1.6 mm and dwell time of 0). The white dashed circle in (f) indicates the deformed metallic volume just below the interface. ....	65
Figure 5.30 Effect of the welding parameter levels on the bonded width: (a) rotational speed, (b) plunge depth, and (c) dwell time. ....	65
Figure 5.31 Hardness profiles comparing: (a) dwell time levels (rotational speed of 1200 rpm and plunge depth of 1.6 mm); (b) plunge depth levels (rotational speed of 1200 rpm and dwell time of 2 s); and (c) rotational speed levels (plunge depth of 1.6 mm and dwell time of 0).....	66
Figure 5.32 Cross section of a tested lap-shear specimen and the respective aluminum fracture surface: (a) and (b) through the interface fracture mode (weld condition: 1200 rpm, 1.6 mm, 0); (c) and (d) transitional fracture mode (weld condition: 2000 rpm, 1.8 mm, 0); (e) and (f) plug pullout with tearing (weld condition: 1500 rpm, 2 mm, 2 s). ....	67
Figure 5.33 Correlation between the LSS and the fracture modes of the Al/Cu friction spot-welded joints. ....	68



- Figure 5.34 Fracture morphology of a plug pullout with tearing fracture mode: (a) Cu fracture surface and (b) Al fracture surface. The two dashed lines shows the boundary of region i and region ii; the dash-dotted line shows the profile of the sleeve..... 69
- Figure 5.35 Fracture morphology of different areas: (a) an overview (marked in Figure 5.34 (a) by a white box), (b) area 01, (c) area 02, (d) area 03 and (e) area 05. Area 01, area 02 and area 03, and area 05 locate at regions i, ii, and iii, respectively. .... 71
- Figure 5.36 Fracture surface correlation of the same area on both sheets at region ii: (a) Cu sheet and (b) Al sheet..... 72
- Figure 5.37 Fracture surface correlation of the same area on both sheets at region i: (a) Cu sheet and (b) Al sheet. .... 73



## SYMBOLS AND ABBREVIATIONS

ANOVA	analysis of variance
ASM	American Society for Metals
ASTM	American Society for Testing and Materials
AWS	American Welding Society
BM	base metal
CF	clamping force, N
CI	confidence index
DF	degree of freedom
DHP	phosphorus-deoxidized
DoE	design of experiments
DT	dwell time, s
EDS	energy dispersive spectroscopy
EBSD	electron backscatter diffraction
F	F-value
FSpW	friction spot welding
FSSW	friction stir spot welding
FSW	friction stir welding
HAZ	heat affected zone
HVAC	heating, ventilation and air conditioning
HZG	Helmholtz-Zentrum Geesthacht
IACS	International Annealed Copper Standard
ISO	International Organization for Standardization
LSS	lap-shear strength, N
MIG	gas-metal-arc-welding
OFAT	one-factor-at-a-time
P	percentage of contribution, %
PD	plunge depth, mm
PT	plunging time, s
Q	energy input, J
RS	tool rotational speed, rpm

RT	retracting time, s
SEM	scanning electron microscopy
SS	sum of squares
SZ	stir zone
TIG	gas-tungsten-arc-welding
TMAZ	thermo-mechanically affected zone
V	variance
WP	work-packages
$\omega$	angular speed, rpm
$\Delta t$	welding time, s

## 1 MOTIVATION

The interest in dissimilar materials welding is consequence of its technical and economic potential benefits. In the case of aluminum and copper (hereafter referred to as Al/Cu) dissimilar welds, the increasing interest is due to the possibility of improving the performance of cable and wiring systems, as well as, heat exchangers and electrical circuits [1]. Aluminum offers an enormous weight and cost saving potentials; however, as Cu presents higher electrical and thermal conductivity, there are applications where a hybrid construction would require welding Cu and Al components together.

The welding technique is regarded as one key factor that many times prevents Al/Cu industrial application. Traditional fusion welding methods are seldom used [2], because differences between physical properties (e.g. melting temperature, thermal conductivity, volumetric specific heat, thermal expansion coefficient, etc.) always generate thermal stress gradients within solidifying welds. Furthermore, solidification of dissimilar metals frequently creates plenty of brittle intermetallic compounds [3].

In contrast with fusion welding, solid-state welding processes offer many advantages, besides the avoidance of problems related to the melting of the materials [3]. Among these processes, friction spot welding (FSpW) is especially appealing.

The FSpW process is an emerging and very attractive technique that has proven to be a potential candidate for spot joining applications, since it overcomes disadvantages commonly observed in other variances of the technology. Regarding the mechanical fastening technique the general problems are: weight penalty; automation difficulty; requirement for sealant; and corrosion problems. Considering the friction stir spot welding (FSSW) process the main limitation is the presence of the key-hole feature [4]. FSpW has already been successfully used to join similar welds of Al or Mg alloys and dissimilar material combinations, such as Al/Mg and Al/Steel [5].



## 2 OBJECTIVES

With the aim of achieving process-specific knowledge concerning friction spot-welded joints of Al/Cu, the following objectives were devised:

- Optimize the process parameters and determine the dominant factors by means of design of experiments (DoE);
- Analyze the microstructure and its formation mechanisms;
- Determine the fracture behaviors of the welds under shear loading.





### **3 LITERATURE REVIEW**

#### **3.1 Literature Survey on the Materials**

##### **3.1.1 Al and Al Alloys**

This section presents an overview of the relevant properties and characteristics of the Al and Al alloys for electric and thermal applications and for the welding industry. Much of the current information is available on the ASM Handbook [6].

###### **3.1.1.1 Al and Al Alloys in Electric and Thermal Applications**

The use of aluminum instead of competing materials in electrical and thermal applications is based on a combination of low cost; good electrical and thermal conductivities; adequate mechanical strength; excellent corrosion resistance; and light-weight.

Compared to copper, aluminum has approximately one-third of copper's density and costs one fourth of its price [7]. Aluminum electrical conductivity is nearly twice that of copper on an equivalent weight basis. For example, the most common conductor alloy, AA1350, offers a minimum conductivity of 61.8 % of the International Annealed Copper Standard (IACS). When compared with IACS on a basis of mass instead of volume, minimum conductivity of hard drawn aluminum 1350 increases to 204.6 %. Aluminum's thermal conductivity is about 50 to 60 % that of copper, which is advantageous in heat exchanges, evaporators, electrically heated appliances and automotive cylinder heads and radiators.

A chart with the material indexes as axis reveals the materials with the optimum combination of heat transfer and mass reduction. Figure 3.1 illustrates this using cast iron for comparison; for an equal weight of mass reduction and heat transfer, aluminum alloys are an excellent choice [8].

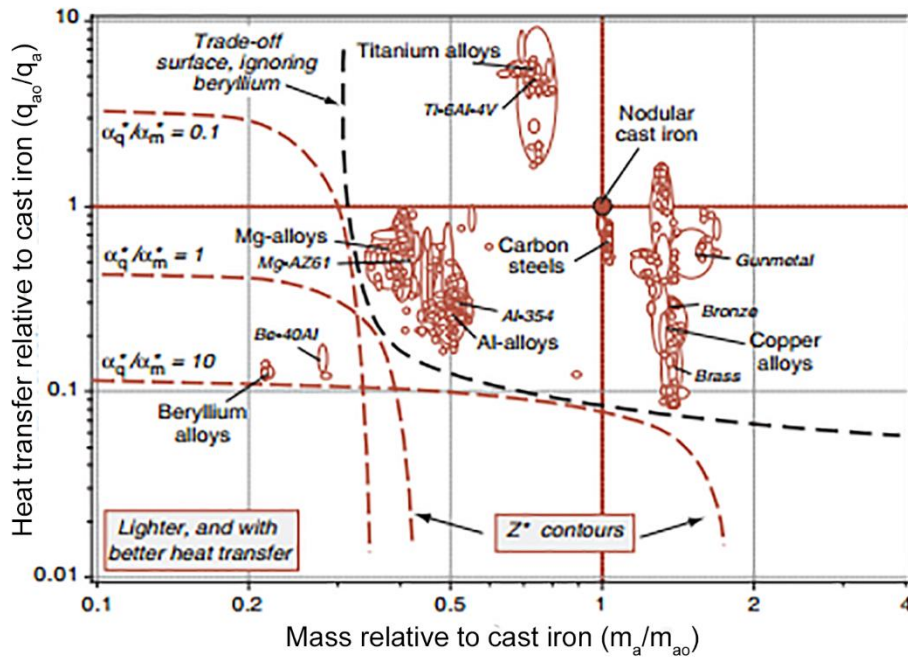


Figure 3.1 Chart with the material indexes normalized by the values of cast iron [8].

### 3.1.1.2 Welding of Aluminum

The two most conventional fusion welding methods suited for aluminum alloys are gas-tungsten-arc-welding (TIG) and gas-metal-arc-welding (MIG), both of which employ inert gases, pure argon or a mix of argon with helium [9]. Before the discovery of these processes, the major issue in welding Al was the formation of aluminum oxide during the process, which has a much higher melting point and electrical isolation in comparison to aluminum bulk material. These oxide fragments cause a reduction in ductility, lack of fusion and possibly weld cracking. For these reasons, even for TIG and MIG techniques, sound metal fusion does not occur unless the prior oxide/hydroxide layer in the surface is removed.

Other obstacles that affect the welding of Al include: high hydrogen solubility in the molten state, which leads to solidification porosity [10]; high thermal conductivity, which demands higher heat inputs in order to keep up with heating; and high electrical conductivity, which requires high currents to produce the same heating effect of steel, for example, in resistance welded joints [11].

Most of the wrought grades in the 1xxx, 3xxx, 5xxx, 6xxx and medium strength 7xxx (e.g. 7020) series can be fusion welded using TIG, MIG and oxyfuel processes. The 5xxx series alloys, in particular, have excellent weldability. High strength alloys (e.g. 7010 and 7050) and most of the 2xxx series are not recommended for fusion welding because they are prone to liquation and solidification cracking [12].

Solid-state welding techniques, particularly the friction stir welding, are strongly suited to aluminum alloys. It is capable of producing sound welds in many alloys, including those heat treatable alloys which are prone to hot cracking during fusion welding [12].

### 3.1.1.3 Aluminum Alloy 5083

One of the materials to be welded in the present work is AA5083-O, provided by the Helmholtz-Zentrum Geesthacht (HZG) research institute.

Although there is no declared application of this alloy in the HVAC segment, the use of this specific alloy was preferred since other studies have already investigated copper and AA5xxx friction stir weldability. Providing, therefore, basic knowledge for this study [13, 14].

Aluminum 5083-O is an annealed wrought alloy of the 5000 series, which has Mg as the main alloying element. The high solubility of Mg in Al enables large additions, and the result is a moderate-to-high-strength work-hardenable alloy [15]. The chemical composition of this material and its main properties are shown in the following tables.

Table 3.1 Typical chemical composition of AA5083-O (weight %) [15].

Al	Cr	Cu	Fe	Mg
Balanced	0.05-0.25	≤0.10	≤0.40	4.0-4.9
Mn	Si	Ti	Zn	Other
0.4-1.0	≤0.40	≤0.15	≤0.25	≤0.15

Table 3.2 Main mechanical, physical, thermal and electrical properties of AA5083-O at room temperature [15].

Mechanical / Physical Properties		Thermal / Electrical Properties	
Modulus of elasticity (GPa)	70.3	Melting Point (°C)	590
Yield tensile strength (MPa)	145	Thermal conductivity (W/m·K)	120
Ultimate tensile strength (MPa)	290	IACS (%)	29
Elongation to fracture (%)	25	Electrical resistivity (nΩ·m)	59.5
Hardness, Vickers (HV0.2)	76		
Density (g/cm <sup>3</sup> )	2.66		

### 3.1.2 Cu and Cu Alloys

This section presents an overview of the relevant properties and characteristics of the Cu and Cu alloys for electric and thermal applications and for the welding industry. Much of the current information is available on the ASM Handbook [6].

#### 3.1.2.1 Cu and Cu Alloys in Electric and Thermal Applications

Copper and its alloys are relatively good conductors of electricity and heat. In fact, Cu is used for these purposes more often than any other metal. It is defined as the electrical conductivity standard of the engineering world, with a rating of 100 % IACS.

Alloying invariably decreases electrical conductivity and, to a lesser extent, thermal conductivity. The amount of reduction due to alloying does not depend on the conductivity or any other bulk property of the alloying element, but it depends on the effect that the particular solute atoms have on the copper lattice

- free electrons in metals are scattered by impurities [16]. For this reason, pure copper and high-copper alloys are preferable when high electrical or thermal conductivity is required for an application.

### **3.1.2.2 Welding of Copper**

The high electrical and thermal conductivities of copper and certain high-copper alloys have a considerable effect on weldability. Welding heat is rapidly dissipated into the base metal and may promote incomplete fusion in weldments. Preheating the copper alloys provides an alternative that reduces the during-weld heat input requirements, necessary to good fusion [17].

Soldering, brazing and welding are the most widely used processes for joining copper metals. Many copper and copper alloys can seldom be welded by other techniques, such as resistance, laser, ultrasonic and friction. Selection of the best welding technique is governed by welding configuration, thickness of the components and alloy composition. Resistance spot welds, for example, can only be performed in copper alloys having an electrical conductivity of 30 % IACS or less, including beryllium copper, many brasses and bronzes, nickel-silver and copper-nickel alloys. Resistance spot welding of unalloyed copper is not practical [17].

Friction based welding processes, although limited in application, offers several advantages. These processes can be used to join copper to itself, to copper alloys and to other metals including aluminum, silver, carbon steel, stainless steel and titanium. Solid-state welding demonstrates excellent applicability specifically for oxygen-free and deoxidized copper [17].

### **3.1.2.3 Phosphorus Deoxidized Copper**

The most common way to catalog copper and copper alloys is to divide them into six families: pure copper, high-copper alloys, brasses, bronzes, copper

nickels and nickel silvers. These alloys are further divided into the wrought and cast alloy categories.

The segregation of oxygen in the grain boundaries causes copper embrittlement [18], therefore most copper alloys are deoxidized. The deoxidizer must have an affinity for the oxygen present in molten copper and be relatively inexpensive compared to copper and any other additions. Lithium, sodium, beryllium, magnesium, boron, aluminum, carbon, silicon and phosphorus can be used to deoxidize Cu.

The copper-pure samples used in this work were sheets of commercial phosphorus-deoxidized (DHP) copper from KME Italy S.p.A. The electrical conductivity of this copper decreases in proportion to the residual phosphorus. When the phosphorus content is 0.009, electrical conductivity is about 100 % IACS. Electrical conductivity is about 85 % IACS for a phosphorus content of 0.02, and electrical conductivity is about 75 % IACS for a phosphorus content of 0.04 [17]. The nominal chemical composition and the main properties of Cu-DHP, available in the material data-sheet [19], are presented in the following tables.

Table 3.3 Nominal chemical composition of Cu-DHP (weight %) [19].

Cu	P
≥99.90	0.015-0.04

Table 3.4 Main mechanical, physical, thermal and electrical properties of Cu-DHP at room temperature [19].

Mechanical / Physical Properties		Thermal / Electrical Properties	
Modulus of elasticity (Gpa)	110	Melting Point (°C)	1083
Yield Tensile strength (MPa)	≥180	Thermal conductivity (W/m·K)	330
Ultimate Tensile strength(MPa)	240-300	IACS (%)	81
Elongation to fracture (%)	8	Electrical resistivity (nΩ·m)	21.7
Hardness, Vickers (HV0.2)	85		
Density (g/cm <sup>3</sup> )	8.9		

### 3.2 Review on Aluminum/Copper and Aluminum/Copper/Magnesium System

Aluminum and copper have a strongly negative mixing enthalpy leading to an easy formation of intermetallic phases [20]. The Al/Cu equilibrium phase diagram is presented in Figure 3.2. It shows on the Cu side a region of high solubility of Al, while on the Al-rich portion low solubility of Cu is demonstrated [21].

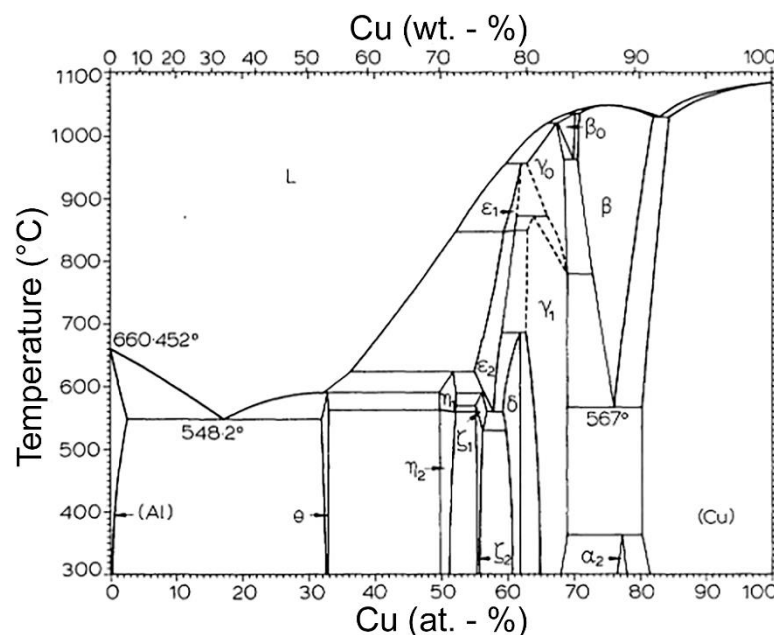


Figure 3.2 Al/Cu binary diagram [21].

This equilibrium phase diagram contains six intermetallic compounds stable at ambient temperature and seven at elevated temperature. An overview of the Al/Cu phases is given in Table 3.5 [22].

One systematic experimental work on the properties of individual Al/Cu intermetallic compounds has been reported by Rabkin et al. [23], who claimed to have isolated the intermetallic compounds by pulling them in vacuum from the appropriate melt. The properties subsequently measured were microhardness, ultimate tensile strength, resistivity and the coefficient of thermal expansion. There is some doubt, however, whether the experimental techniques employed by Rabkin et al. could have produced just a single intermetallic rod rather than a rod consisting of several intermetallic compounds. The doubt arises from the

basis of solidification theory, which states that: even with a high cooling rate from the molten state, several solid intermetallic compounds would grow and not just one. Nevertheless, their results indicated that the various intermetallic phases (or intermetallic phase mixture) were brittle and present high electrical resistance [24].

Table 3.5 Composition information of the Al/Cu binary system compounds, according to Ponweiser [22].

Phase	Composition range [21]
(Al)	0-2.48
$\Theta$	31.9-33.0
$\Pi_1$	49.8-52.4
$\Pi_2$	49.8-52.3
$\zeta_1$	55.2-59.8
$\zeta_2$	55.2-56.3
$\epsilon_1$	59.4-62.1
$\epsilon_2$	55.0-61.1
$\delta$	59.3-61.9
$\gamma_0$	59.8-69
$\gamma_1$	52.5-59
$\beta_0$	67.6-70.2
$\beta$	70.6-82.0
$\alpha_2$	76.5-78
(Cu)	80.31

These properties imply that significant intermetallic growth at the interface during the welding process can weaken the welded joint and act as the major cause of failure. The intermetallic formation would also have an adverse effect on the electrical stability of the equipment, since it drastically increases the resistivity.

Fortunately, only two or three intermetallic phases ( $\text{Cu}_9\text{Al}_4$ ,  $\text{CuAl}$  and  $\text{CuAl}_2$ ) typically show up in rotary friction welding, friction stir welding, diffusion welds and diffusion couples of this system [25].

The presence of magnesium as the main alloying element in the 5000 series leads to solute hardening of the alloy and efficient strain hardening. Not only is



Mg a very effective solid solution strengthening element in terms of its effect per weight in solution, but also its high solubility in aluminum enables large additions of the element. Alloys in the 5000 series may contain from about 0.5 to 6 wt% Mg in the most highly alloyed variants [6]. Therefore, this high content level of magnesium in the AA5000 series should be taken in consideration in this study.

The Al-Cu-Mg equilibria is complex, with four well-defined, but several less-well-defined ternary phases governing the solid-state phase equilibria. The four well-defined ternary phases are designated in the literature as Q, S, T and V phases, which are based on the following compositions:  $\text{Cu}_3\text{Mg}_6\text{Al}_7$ ;  $\text{CuMgAl}_2$ ;  $(\text{Cu}_{1-x}\text{Al}_x)_{49}\text{Mg}_{32}$ ; and  $\text{Cu}_6\text{Mg}_2\text{Al}_5$ , respectively [26].

These equilibrium phase diagrams provide the basis for initial analyses; however, the formation of intermetallic phases cannot be exclusively understood based on the Al/Cu or Al/Cu/Mg phase diagrams, since the chemical reactions occurring under the thermal cycles imposed by the FSpW process are far from the equilibrium conditions [13].

### **3.3 Friction Spot Welding**

#### **3.3.1 Process Description**

FSpW is a spot-like solid-state welding technology used for producing similar and dissimilar overlap welds in different classes of materials, such as aluminum, magnesium, steel and thermoplastics [4]. This process does not require additional connection elements and is reproducible with high precision and in a simple manner [27].

FSpW was derived from FSW, which was patented in 1991 by The Welding Institute and has already achieved a mature stage for industrial application. The transverse movement of the tool does not occur during the FSpW process; just the pin and the sleeve, components of the FSpW tool, move axially through the material.

The process, patented in 2000 by the HZG research institute, consists of four stages performed by a non-consumable cylindrical tool composed of three components, the clamping ring, sleeve and the pin, assembled co-axially, as shown in Figure 3.3 [28].



Figure 3.3 Schematic illustration of the three-piece tool system used in the FSpW process [28].

The pin and the sleeve are controlled by separate actuators in a way that allows them to move upwards and downwards independently. The clamping ring is a non-rotational component that holds the sheets to be welded against the backing rod during the process and also provides an outer wall, which prevents the outflow of plasticized material.

The process allows two variants, one where the sleeve penetrates the material and another where is the pin that does. The sleeve penetration, compared to the pin penetration, results in a larger welded area; therefore, the mechanical resistance achieved is higher. On the other hand, pin penetration variant is easier to perform since it demands less power associated with lower frictional forces [4]. In this variant the stir zone is deeper, which could constitute an obstacle mainly in cases of dissimilar materials welding.

In the sleeve penetration variant, Figure 3.4, first the sleeve and the pin start to rotate in the same direction under a pre-set speed (Figure 3.4 (a)). Then the sleeve is forced against the upper sheet, generating frictional heat that leads to a volume of plasticized metal, while the pin moves axially in the opposite direction, creating a cavity where the plasticized material is displaced and stored (Figure 3.4 (b)). When the desired penetration depth is achieved, the process is reversed and both the pin and the sleeve retract back to the surface of the upper-

sheet (Figure 3.4 (c)) in such a way that the plasticized metal is pushed back into the workpiece. Finally, after the completion of the weld, the welding tool is removed, resulting in a flat surface connection without material loss (Figure 3.4 (d)).

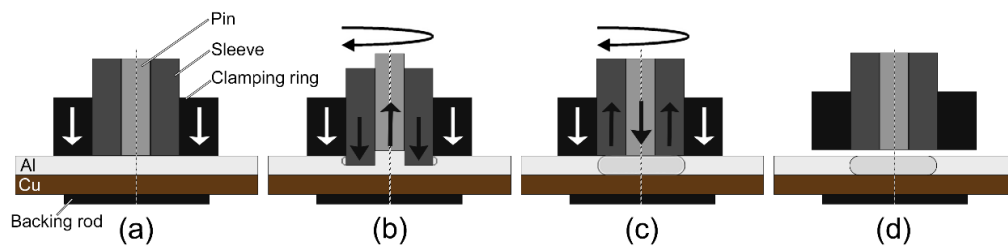


Figure 3.4 Schematic representation of the FSpW process - sleeve penetration variant: (a) clamping and spindle rotation; (b) sleeve plunges into the upper sheet while the pin moves upward; (c) spindles retract back and (d) withdrawal of the welding head.

The main improvement of the FSpW over FSSW, another FSW process variant, developed in 1993 by Mazda Motor Company, is the absence of the key-hole feature in the spot seam. This characteristic of the FSpW process usually leads to higher weld strengths due to the reduction of the geometrical notch effect.

Moreover, when compared to mechanical fastening (clinching, riveting, self-piercing rivet) and resistance spot welding, which are frequently applied as spot joining and welding methods, better characteristics were noted in the FSpW process. Mechanical fastening has as disadvantages the weight penalty, difficulty of automation, necessity of sealants and corrosion issues [4]. When considering resistance spot welding, one important disadvantage is the elevated energy required for welding aluminum alloys, which increases the operational cost [29]. FSpW also presents many other advantages over fusion welding technologies. It results in a weld with fewer defects, such as voids, cracks and other distinct defects throughout the weld that are related to the material fusion. Furthermore, regarding the welding of aluminum, there is no requirement for chemical cleaning processes to remove the oxide/hydroxide layer from the surface.

The energy efficiency, environmental friendliness and versatility make the FSpW process a promising technology to join several structural components.

### 3.3.2 Process Parameters

The parameters involved in the FSpW process, which influence the material flow and temperature profiles and therefore, are responsible for the mechanical and metallurgical characteristics of the welds, are:

- Tool rotational speed (RS) - the speed at which the tool spins, in rotations per minute. The rotation of the tool results in the stirring and mixing of material in the stir zone. Higher tool rotational speeds generate higher temperature input into the weldments due to higher frictional heating, and also result in a more intense material mixing.
- Plunge depth (PD) - defined as the depth that the plunging element reaches, after passing through the original surface of the top of the workpiece. It not only strongly affects the weld strength and the failure mode, but also influences the appearance of the weld [30]. One of the main differences in the process parameters of dissimilar FSpW, compared to those applied in similar FSpW, is that the tool plunge remains on the top material sheet in the former.
- Plunging time (PT) - the time required for the plunging element to achieve the desired PD. It has practically no effect on the strength of the weld [31], however a longer time causes time expenditure, resulting in a lack of production.
- Retracting time (RT) - the time required for the plunging element to retract to the surface of the sheet. A longer time is at the expense of production efficiency.
- Dwell time (DT) - defined as the time during which the plunging element is held at the desired plunge depth. A longer dwell time ensures a proper material mixing and increases the volume of deformed material, resulting in a larger stir zone. However, a shorter dwell time results in a lower welding time, making the process more attractive for industrial applications.
- Clamping force (CF) - the force that the clamping ring applies to hold the materials against the backing rod during the welding process. Higher clamping forces could result in a deeper surface indentation, which is not desirable for spot welding.
- Tool geometry - tool design is known to be a critical component to develop suitable welds [32]. The presence of the thread seems to have a negligible effect

on the amount of energy generated during FSSW compared to a non-threaded geometry [33]. A threaded tool, although not strong in terms of wear, enhances the material flow and could result in higher weld strengths.

### 3.3.3 Energy Input

According to Su et al. [33, 34], the energy input during FSSW, in which heat generation is similar to the FSpW process, is determined by Equation 3.1:

$$Q = \sum_n^{n=N} Force(n)(x_n - x_{n-1}) + \sum_n^{n=N} Torque(n)\omega(n)\Delta t \quad 3.1$$

The total heat input ( $Q$ ) is equal to the sum of the heat input from the axial load contribution and the frictional contribution;  $n$  is the increment under consideration and  $N$  is the final increment. The axial load contribution is a function of the force and the plunge depth of the tool ( $x_n - x_{n-1}$ ) and the frictional contribution depends on the torque, the angular speed ( $\omega$ ) and the welding time ( $\Delta t$ ).

Su et al. [35] reported the friction contribution to be around 200 times higher than the axial load contribution. Therefore, it is common, as a simplification, to ignore the first part of Equation 3.1 and assume that the energy is associated only with torque, angular speed and welding time. It was also identified that only a small percentage of the total energy generated during the process is required for stir zone formation [33]. The majority of the energy is dissipated as heat to the tool assembly, to the clamping system, to the plates being welded and to the surrounding atmosphere.

A drop in the heating generation efficiency can take place when higher tool rotational speeds are applied, since the torque decreases due to the slippage of the tool and the plasticized material. This phenomenon can be observed in Figure 3.5 [33].

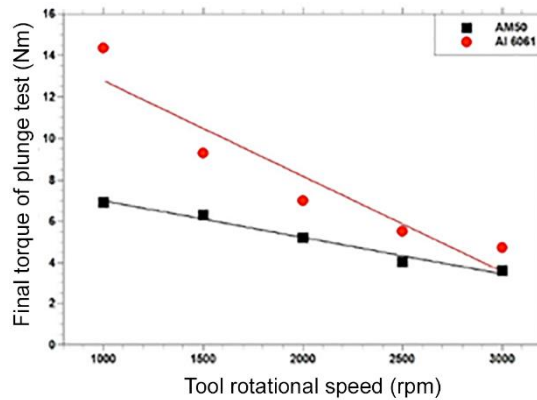


Figure 3.5 Relation between the tool rotational speed and the torque during FSSW of AA6061 and AM50 [33].

A strong positive correlation was found between the energy input, the size of the bonded area and the failure load, as shown in Figure 3.6 [35]. The fracture load increases with the increase of the energy input and bonded area.

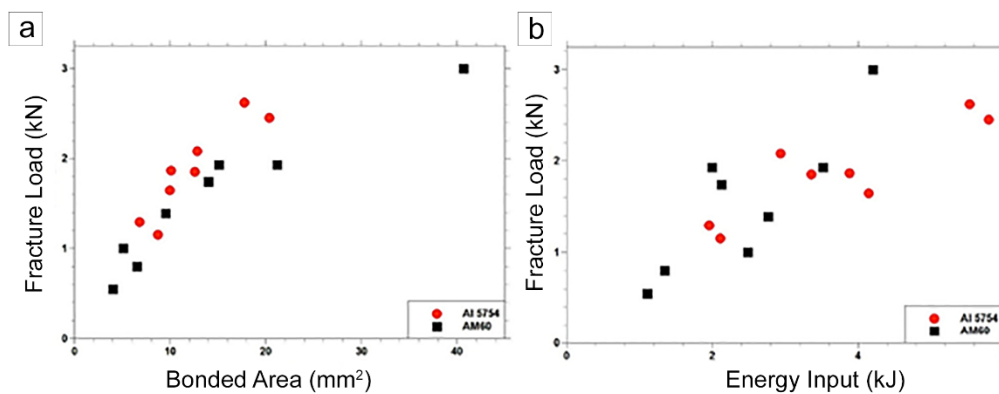


Figure 3.6 Weld strength as function of (a) bonded area and (b) energy input [35].

Besides the mechanical strength of the weld, the size of the bonded area also affects the failure mode, as reported by Chang et al. [36]. It was observed that higher bonded areas present failure modes associated with high energy absorption, while welds with low bonded areas failed in a brittle manner as shown in Figure 3.7 [36].

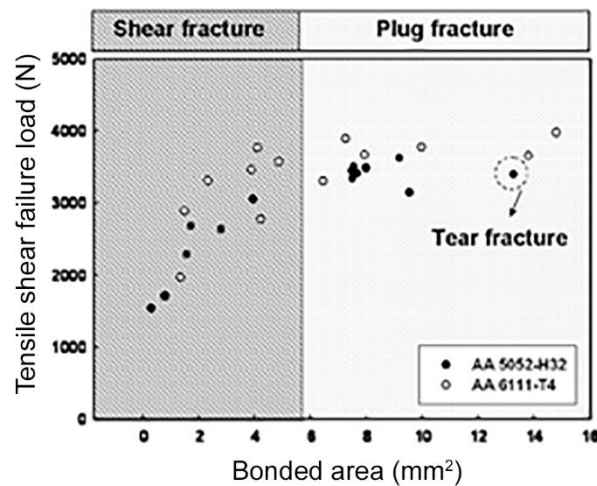


Figure 3.7 Weld strength and fracture modes as function of bonded area [36].

Although it is generally accepted that a higher heat input provides better mechanical properties, this could be an obstacle when welding dissimilar materials, due to the fact that a higher heat input can induce a higher quantity of intermetallic compounds, which are usually brittle, causing a drop in strength [37].

### 3.3.4 Characterization of the Welding Zones

During the FSpW process, temperature and plastic deformation generate a significant microstructural change. These changes, as in FSW, could involve grain size, grain boundary character, dissolution and coarsening of precipitates, breakup and redistribution of precipitates, as well as texture modification within and around the stirred zone [38].

Based on microstructural characterization, three distinct zones have been identified: stir zone (SZ), thermo-mechanically affected zone (TMAZ) and heat affected zone (HAZ). Although the HAZ is not easily distinguished by optical microscope, hardness test results indicate the presence of this region. The three distinct welding zones and the respective hardness profile are identified in Figure 3.8 [39].

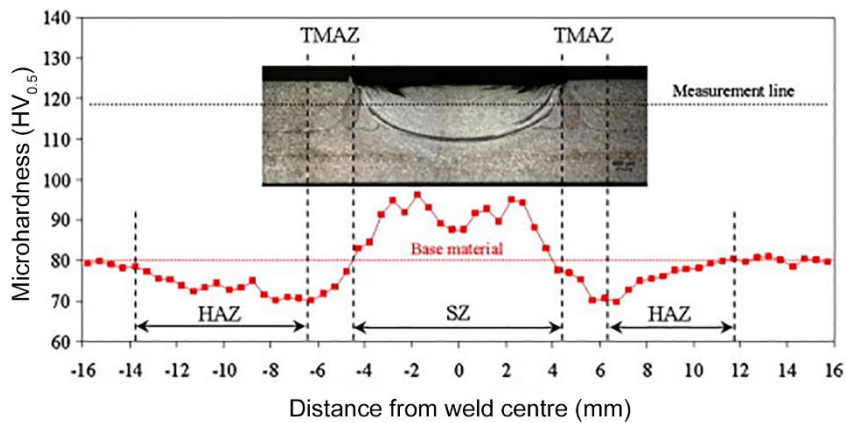


Figure 3.8 Cross section macrograph and hardness profile of an AA6181 friction spot-welded joint [39].

The difference between the welding zones taking in consideration the size and shape of the grains are illustrated in Figure 3.9 (a).

The SZ experiences intense plastic deformation and frictional heating during the process, resulting in a dynamically recrystallized fine-grained microstructure, as illustrated in Figure 3.9 (b) [39].

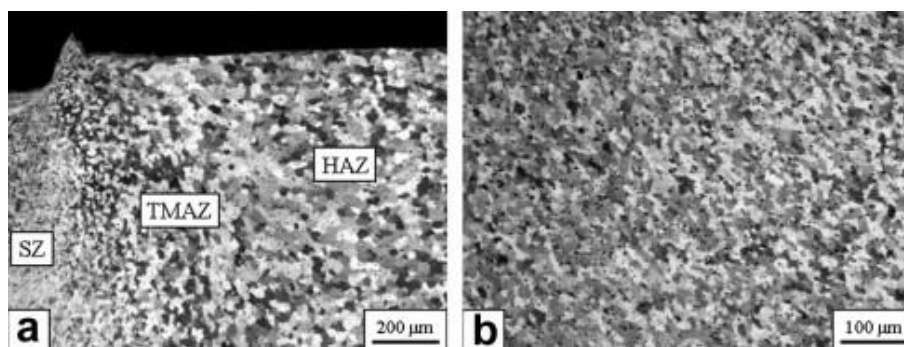


Figure 3.9 Optical microscope images of the distinct welding zones in AA6181 friction spot-welded joints (a) deformed grains in the TMAZ and (b) refined microstructure in the SZ [39].

The TMAZ is a transition zone between the SZ and HAZ, as illustrated in Figure 3.9 (a). This region experiences both heating and plastic deformation; however, in a lower intensity level when compared to the SZ. Therefore, recrystallization does not occur due to insufficient deformation [40]. The result depends on the material properties, recovery usually occurs and, eventually, destabilization of the heating treatment of the alloy [41].



The HAZ is a transition zone between the TMAZ and base metal. In this region, the temperature achieved modifies the microstructure and/or the mechanical properties. However, there was no plastic deformation occurring in this region.

Some authors consider one fourth zone, the mixed zone also known as intermixed zone [42]. This zone, formed inside the SZ, is particularly visible in dissimilar welds and consists of intermittent slices of each welded material. Figure 3.10 shows, in detail, the intermixed zone.

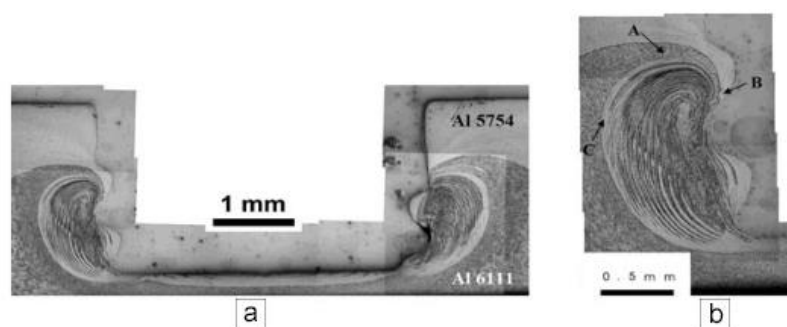


Figure 3.10 FSSW of dissimilar AA5754/AA6111 (a) macrograph and (b) intermixed zone [42].

### 3.3.5 Fracture Behavior under Shear Loading

Three main fracture modes, as shown in Figure 3.11, are commonly observed in FSpW: (a) through the interface, (b) plug pullout with tearing and (c) plug pullout [39].

Through the interface failure mode is associated with crack propagation along the SZ and parallel to the overlap interface. Although in Figure 3.11 (a) this fracture mode is accompanied with a circumferential crack, this does not usually happen [41]. This mechanism is commonly associated with catastrophic brittle fracture of the welded joint. However, in some types of spot welds, this fracture mode can result in high lap-shear strength and intermediate ductility [4].

The plug pullout with tearing fracture mode, as seen in Figure 3.11 (b), also called debonding, is associated with the propagation of a crack along the boundary of the welding zones. It does not necessarily involve tearing [41].

In the plug pullout fracture mode, as illustrated in Figure 3.11 (c), the plug can remain partially connected to the upper or lower plate or can be completely removed [41]. This is a typical fracture mode found in sound friction spot welds. Welds that exhibit this mechanism fail in a ductile manner; in other words, they are usually associated with excessive plastic deformation in the vicinity of the fracture as well as dimples at the fracture surface.

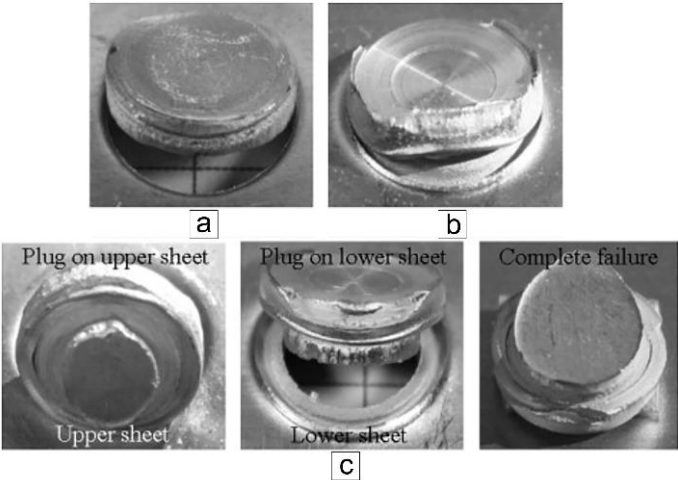


Figure 3.11 Friction spot-welded joints fracture modes in lap-shear tensile test: (a) through the interface, (b) plug pullout with tearing and (c) variants of plug pullout [39].

The fracture mode has an important influence on the amount of energy absorbed during fracture. Experience has shown that, for almost the same failure load, the plug pullout fracture modes are associated with higher energy absorption prior to failure when compared to the through the interface failure mode, as shown in Figure 3.12 [4].

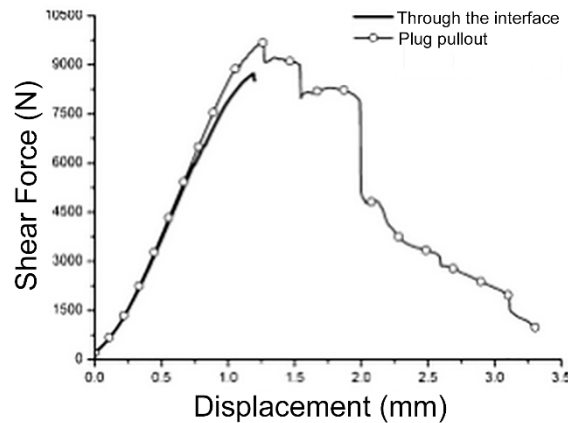


Figure 3.12 Force vs. displacement curve observed during lap-shear testing of friction spot-welded AA2024 [4].

### 3.4 Design of Experiments

There are many factors that are known to affect the lap-shear strength (LSS) of the friction spot-welded joints, therefore a DoE technique becomes very important to analyze this as a process response. DoE is a powerful statistical tool often applied in industrial process optimization and analysis to systematically investigate the process or product variables that influence product quality [4]. Various optimization methods can be selected for this purpose.

The Taguchi method is one simple and robust DoE technique usually selected due to its good compromise between the amount of experiments required and the resolution. The Taguchi method provides a range of experimental arrays, developed on a statistical basis to ensure a balanced comparison of levels of any factor. However, due to the necessary assumptions and simplifications, this method may not clearly explain the effects of all the second and third order interactions between variables. An interaction occurs when the effect of one input variable is influenced by the level of another input variable. Therefore, the Taguchi-type design should be considered only as a screening type of experiment, which will usually find the most significant individual process parameters [43]. This can be accomplished by using an analysis of variance (ANOVA) technique, dividing two variances and comparing the ratio to a value

found in the literature. ANOVA can also determine the relative contribution, expressed as a percentage, which each controlled parameter makes to the overall measured response. The calculations involved in the ANOVA technique are described below [44]:

$$SS_T = \sum_i^m n_i^2 - \frac{1}{m} \left[ \sum_{i=1}^m n_i \right]^2 \quad 3.2$$

where  $SS_T$  is the total sum of squares,  $m$  is the total number of experiments and  $n_i$  is the experimental result for the  $i^{th}$  experiment;

$$SS_p = \sum_{j=1}^t \frac{(S_{n_j})^2}{t} - \frac{1}{m} \left( \sum_{i=1}^m n_i \right)^2 \quad 3.3$$

where  $SS_p$  represents the sum of squares from the tested factors,  $p$  is one of the tested factors,  $j$  is the level number of this specific factor  $p$ ,  $t$  is the repetition of each level of the factor  $p$  and  $S_{n_j}$  is the sum of the experimental results involving this factor  $p$  and level  $j$ ;

$$V_p = \frac{SS_p}{DF} \quad 3.4$$

where  $V_p$  is the variance from the tested factors and  $DF$  is the degrees of freedom for each factor.

The F-value for each factor is simply the ratio of the variation between the sample means to the variation within the samples, as demonstrated below:

$$F_p = \frac{V_p}{V_{error}} \quad 3.5$$

Lastly, the percentage of the contribution of each individual factor to the total variation can be calculated as follows:

$$P_p (\%) = \frac{SS_p}{SS_T} \times 100 \quad 3.6$$

Another optimization method is the one-factor-at-a-time (OFAT) planning, in which the experimenter seeks to gain information about one factor in each experimental trial. This procedure is repeated in turn for all factors to be studied [45]. Although less statistically efficient, this technique allows the improvement of a baseline set of factor levels through a relative simple experimental plan.

To really estimate the important factors and interactions, a complete factorial or a fractional factorial, with a higher resolution, is usually recommended [43]. In

a full factorial experiment, each factor is tested at each level in every possible combination with the other factors and their levels. Therefore, the number of runs goes up exponentially as factors are added. In order for this experiment to be considered economic and practical, there should be few factors with low number of levels. The advantage is that all paired interactions can be studied.



## 4 MATERIALS AND METHODS

This chapter describes the experimental procedure of the present work. The first part of the procedure was carried out by performing friction spot welding on sheets of AA5083 and Cu-DHP with the dimensions 100 x 25 x 2 mm.

Mechanical characterization of the base materials revealed that the aluminum alloy is softer than the copper. Furthermore, the thermal conductivity of AA5083 is less than half of that of Cu-DHP. Therefore, it is possible to assume that thermal softening is stronger for the aluminum alloy. This extremely soft aluminum alloy could be strongly pushed upwards, if it was positioned as bottom sheet. To avoid such displacement, that could create geometrical and metallurgical defects, the Al sheet was placed on the top of the Cu sheet.

Specimens were produced from the welds in order to characterize them, both metallurgically and mechanically. The mechanical resistance were assessed by LSS and Vickers hardness tests. The metallurgical features were determined by macro and microscopic analyses.

### 4.1 Joining Equipment and Procedure

The Al/Cu friction spot-welded joints were performed at the HZG research institute using the sleeve penetration variant of the process, with a commercially available machine, RPS 100, manufactured by Harms & Wende GmbH & Co.KG, Figure 4.1 [46]. The machine can achieve a maximum axial force of 20 kN and a rotational speed of 3300 rpm. It is possible to monitor the plunge depth, rotational speed, welding time and axial force parameters during the process.

Two different tools were used in this study, one of a threaded and other of a non-threaded geometry, both made of H0TVAR, a high performance molybdenum-vanadium alloyed hot-work tool steel [47]. The tool is comprised of three parts: clamping ring, sleeve and pin with diameters of 14.5, 9 and 6 mm, respectively.

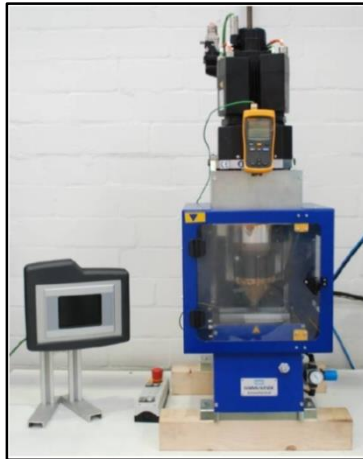


Figure 4.1 RPS 100 FSpW machine used to produce Al/Cu welds [46].

Prior to welding, the base metals were cleaned with acetone in order to remove any machining fluids, and a clamping system was used to firmly fix the sheets against the backing rod, as shown in Figure 4.2.



Figure 4.2 Clamping system used to fix the sheets against the backing rod.

## 4.2 Welding Parameters

The welding parameters: force; sleeve plunge time; sleeve retraction time; and tool geometry were established after an initial screening process, which will be further discussed. The variation of the potentially influential variables: tool rotational speed; plunge depth; and dwell was defined as follows:



Table 4.1 Welding parameters variation.

Factors	Levels		
	Level 1	Level 2	Level 3
Tool rotational speed (rpm)	1200	1500	2000
Plunge depth (mm)	1.6	1.8	2
Dwell time (s)	0	1	2

The PD was fully located in the aluminum plate in order to avoid the formation of a thick layer of brittle intermetallic compounds [20]. These low levels of DT were chosen with the objective of minimizing the welding time. Finally, these levels of RS were defined based on a previous study of Al/Cu FSSW [25].

### 4.3 Mechanical Characterization

#### 4.3.1 Lap-shear Testing

Lap-shear strength was chosen to evaluate the weld quality since this test is a good indicator of the weld properties. In order to give statistical significance to the results, at least three repetitions for each welding condition were done for this DoE. The tests were carried out in accordance with the Standard ISO 14273:2000 [48]. The tensile specimen is shown in Figure 4.3.

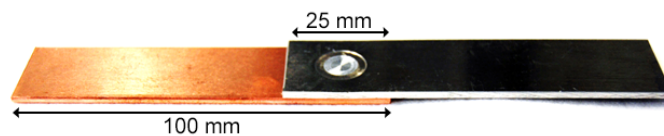


Figure 4.3 Al/Cu friction spot-welded sample for lap-shear testing.

A universal testing machine, Zwick/Roell 1478, performed the lap-shear test at room temperature and at a constant crosshead speed of 1 mm/min. Figure 4.4 shows the lap-shear test machine. Shims of the same material and thickness as the test specimens were used when clamping the samples to avoid twisting.



Figure 4.4 Machine Zwick/Roell used for lap-shear test.

### 4.3.2 Microhardness Testing

The microhardness test is important in providing information about the local mechanical resistance of the base metals and the welding zones. The microhardness measurements were carried out on the as-polished samples, in accordance with the Standard ASTM E384-11 [49], by applying a 0.2 kgf during 10 s and at distance of 200  $\mu\text{m}$  between each indentation. The microhardness profiles were made at the middle thickness of the Al sheet.

### 4.4 Metallurgical Characterization

The metallographic characterization was performed on the cross section of the welds.

The samples were first cut by an  $\text{Al}_2\text{O}_3$  and SiC wheel, in a position near to the center of the weld. Afterwards, the samples were cold mounted and submitted to conventional procedures of grinding and polishing, as described in Table 4.2.

After the grinding and polishing procedures, the samples were immersed at room temperature for 45 s in a Dix-Keller etchant,  $\text{H}_2\text{O}:\text{HNO}_3:\text{HCl}:\text{HF} = 190:5:3:2$ . The chemical etching method fully etched the Al sheet without affecting the Cu one.

Table 4.2 Grinding and polishing procedures.

	Step				
	Grinding		Mechanical polishing		Chemical polishing
Surface	# 320 SiC Paper	MD - Largo	MD - Dac	MD - Nap	MD-Chem
Lubricant/ Abrasive	Water	Diamond solution			Colloidal silica
		9 $\mu\text{m}$	3 $\mu\text{m}$	1 $\mu\text{m}$	0.04 $\mu\text{m}$
Time	3 min	3 min	4 min	2 min	30 s

Immediately after etching, the macroscopic analyses were performed using an optical microscope. With these analyses, the macroscopic features of the welds were evaluated and correlated to the parameters applied and to the results obtained by mechanical testing. The microscopic features were inspected by a scanning electron microscope (SEM) equipped with an energy dispersive spectrometer (EDS) and by the electron backscatter diffraction (EBSD) technique.

The *Thermocalc* software which performs thermodynamic and phase diagram calculations for multi-component systems was run in order to acquire a better understanding of what compounds might possibly be formed during welding.

#### 4.5 Temperature Measurements

The measurements of the temperature cycle developed during the FSpW process were carried out for specific welding conditions. For each condition at least two measurements were performed. The thermometry system consisted of a K-type thermocouple with diameter of 0.5 mm connected to a data acquisition system and controlled by the software Labview, which provided temperature diagrams with a frequency of 50 Hz.

Two thermocouples were positioned in the copper sheet at a depth of 2 mm from the bottom surface, one at a position to measure the temperature achieved

by the center of the pin and the other at a distance of 4.5 mm from the weld center, as illustrated in Figure 4.5.

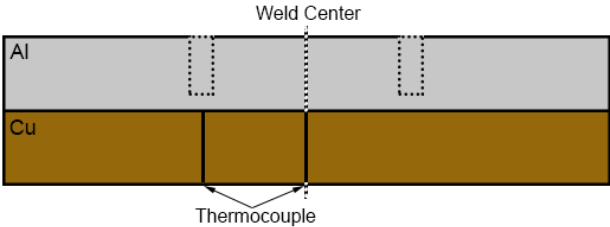


Figure 4.5 Schematic illustration of the thermocouple positioning, superimposed with the tool profile.

**4.6 Research Methods**

The research hereby established has been divided in the following work-packages (WP):

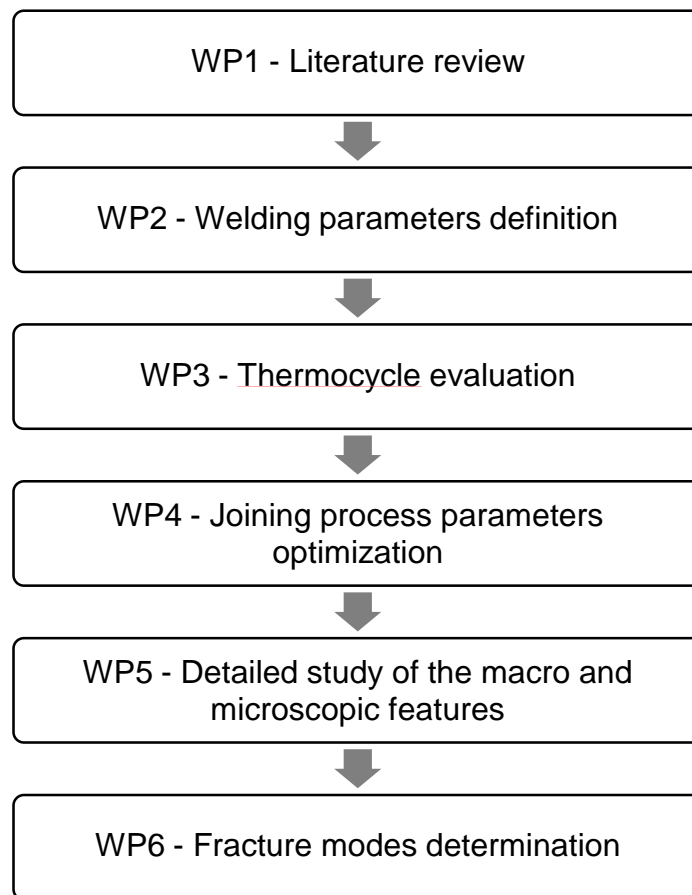


Figure 4.6 Work-packages established for this work.

The initial stage of the research, WP1, consisted of an in-depth literature review regarding the materials and the process.

In WP2, the range of welding parameters was established according to the mechanical performance results obtained by means of lap-shear tests and also according to the macroscopic analyses, which investigated the surface finishing, occurrence of flow defects and the presence of intermetallic compounds. This procedure was important to better understand the process and to define the window of parameters in which a void-free welded joint can be achieved.

The WP3 consisted of a detailed assessment of the energy input being converted into heat, which is then conducted into the plates being welded, according to the welding parameters. Thermocouples were positioned at two different locations inside the copper plate so as to obtain the temperature reached at the weld center and at the edge of the sleeve.

In WP4, three different DoE techniques were selected to organize and analyze the experiments. This procedure overcomes specific disadvantages of each individual approach and allowed a minimization of the number of experiments needed. Taguchi and OFAT methods were used to analyze the influence of the individual process parameters and to optimize the selected response. A third statistical model, designated as full factorial design, was used to quantify the influence of the parameter interactions. Each combination of the experimental factor levels was evaluated by lap-shear testing.

To analyze the typical macro and microscopic features, both optical microscope and SEM were used in the WP5. To obtain a detailed information about the microstructure formation mechanism, a stop-action experiment was carried out. In the stop-action experiment, the welding cycle was forced to stop during one of the process stages. The *Thermocalc* software was used to determine the constituents that would form if the amount of Cu mixed to the Al substrate was of 20, 25, 30, 35, 40 and 45 %. The EBSD technique was also used to identify the phases, which were beyond the spatial resolution of EDS, by indexing the Kikuchi patterns. Microhardness measurements were performed to precisely delimitate each welding zone. The welds' macroscopic features were directly correlated to the mechanical tests.

In the WP6, the fracture modes were identified and correlated to the LSS. Finally, the fracture surface of a sound weld was characterized by means of SEM and the local chemical compositions were assessed via EDS technique.

## 5 RESULTS AND DISCUSSIONS

### 5.1 Screening Stage

Friction spot-welded Al/Cu dissimilar joints have not been previously reported by other researchers. Therefore, a preliminary set of experiments was done before the start of a robust DoE, with the objective to achieve an initial understanding of the process. It was also important to define the window of parameters in which a void-free and a mechanically reasonably sound weld could be obtained.

As mentioned in Section 3.3.3, the size of the bonded area is one factor that significantly influences the mechanical strength of the weld. The bonded area can simply be measured by the bonded width, which comprises the diameter of the SZ circumference. The two possible measurement procedures are illustrated in Figure 5.1. In this work, the bonded width was measured at the fracture surface.

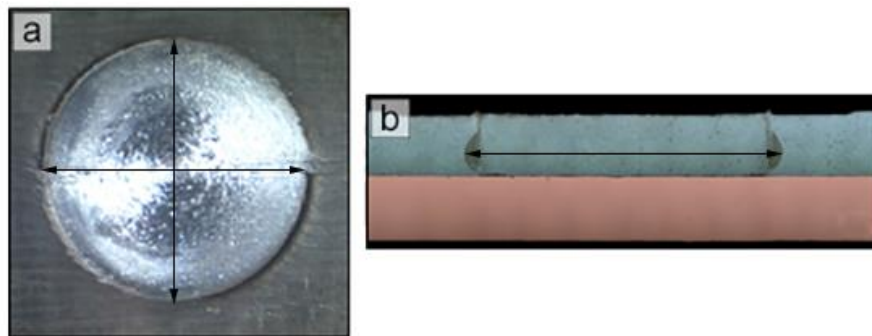


Figure 5.1 Bonded width measurement procedures, according to the: (a) fracture surface and (b) cross section of the welded joint.

#### 5.1.1 Influence of the Tool Geometry

It is well known that the tool design is a critical component to develop suitable welds in the friction-based processes. One of the most interesting issues is the profiled geometry, threaded or non-threaded. The presence of a thread on the tool seems to have negligible effect on the amount of energy generated during

FSSW compared to a non-threaded tool [33]. However, there are both positive and negative aspects when considering the presence of thread. Its presence could facilitate the material flow and relieve possible welding defects, but it is a weak point in terms of tool wear.

In this study, two different tools were used; both are shown in Figure 5.2. With the exception of the threaded profile, all the other geometrical features were the same.

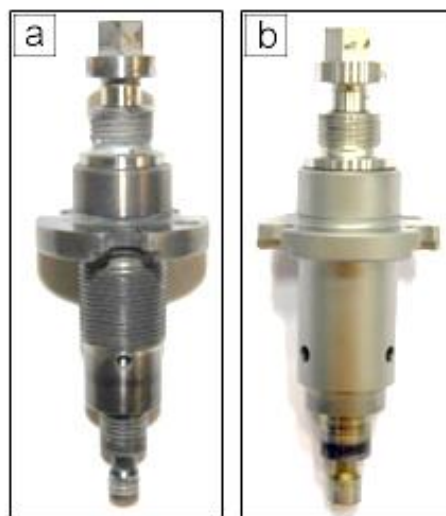


Figure 5.2 FSpW tools used to optimize the process: (a) threaded and (b) non-threaded geometries.

As shown in Table 5.1, the weld produced by the threaded tool has a wider bonded width compared to the one produced by the non-threaded tool. Moreover, although the sleeve penetration applied was the same, the effective plunge depth is deeper for the threaded geometry, since there is an obviously deformed metallic volume under the interface, indicated by the white dashed circle in Figure 5.3 (a). The non-threaded geometry presents a relatively flat interface. These observations more than likely mean that a threaded tool can induce a more effective material flow during welding, which considerably increases the weld strength, as shown in Table 5.1.



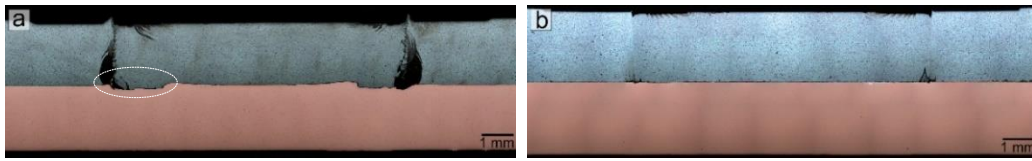


Figure 5.3 As-etched macrographs obtained with a (a) threaded and (b) non-threaded tool. White dashed circle in (a) indicates the deformed metallic volume under the interface. Welding condition: RS = 1200 rpm, PD = 2 mm, DT = 1 s, CF = 17.48 kN, PT = 2 s, RT = 1 s.

Table 5.1 Influence of a threaded and non-threaded geometry on the LSS and respective fracture surface diameter. Welding condition: RS = 1500 rpm, PD = 2 mm, DT = 2 s, CF = 17.48 kN, PT = 2 s, RT = 1 s.

Presence of thread on the tool	LSS (kN)				Fracture surface diameter (mm)
	1	2	3	Average	
Yes	6.91	7.15	7.19	7.09	9.75
No	4.29	3.73	3.98	4.00	8.51

In these experiments, relevant tool wear was not detected in either case. Therefore, for the following experiments, a thread-profiled tool was adopted.

### 5.1.2 Influence of the Clamping Force

As previously described, the CF is the force that the clamping ring applies to hold the base metal sheets against the backing rod during the welding process. Higher clamping forces would result in a deeper surface indentation, which is not desirable for spot welding. On the other hand, lower clamping forces would reduce the heat input, according to Equation 3.1, and therefore the LSS.

As shown in Figure 5.4, although the depth of the surface indentation increases with the CF, the maximum indentation depth does not overcome 10 % of the sheet thickness, which is acceptable according to the Standard AWS D17.2 [50]. In contrast, as shown in Table 5.2, welds with higher LSS were produced by increasing the CF from 14.56 kN to 17.48 kN. Accordingly, a CF of 17.48 kN was used for the further investigations.

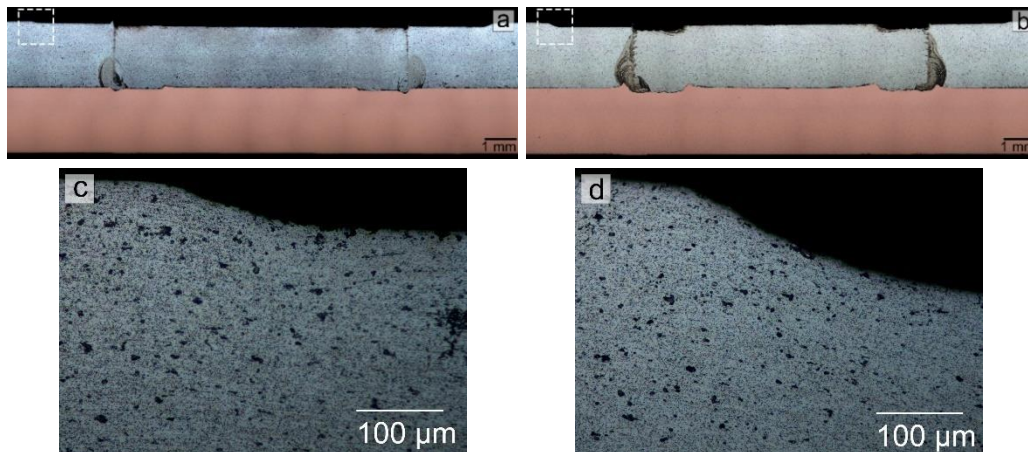


Figure 5.4 As-etched macrographs obtained with a CF of (a) 14.56 kN and (b) 17.48 kN. Magnified view taken from the indentation: (c) location marked with a white box in (a) and (d) location marked with a white box in (b). Welding condition: RS = 1200 rpm, PD = 2 mm, DT = 2 s, PT = 2 s, RT = 1 s.

Table 5.2 Influence of the CF on the LSS and respective fracture surface diameter. Welding condition: RS = 1200 rpm, PD = 2 mm, DT = 2 s, PT = 2 s, RT = 1 s.

CF (kN)	LSS (kN)				Fracture surface diameter (mm)
	1	2	3	Average	
14.56	5.31	4.99	5.01	5.10	8.59
17.48	7.37	6.90	7.04	7.10	9.53

### 5.1.3 Influence of the Sleeve Plunge Time and Retraction Time

As mentioned in Section 3.3.2, the PT has practically no effect on the strength of the welds and normally, longer PT is just at the expense of production efficiency. However, a longer PT would facilitate the heat accumulation, which is helpful for welding materials such as copper, which have high heat conductivity.

When a PT of 1 s was applied, voids were observed close to the sleeve-plunge area, as shown in the as-polished samples in Figure 5.5 (a). This defect is usually associated with insufficient material flow caused by insufficient heat input [51]. However, even after increasing the heat input by increasing the RS, cavities were still found in the samples. When the PT was increased to 2 s, a proper mixing occurred and a void-free weld was obtained, as shown in the Figure 5.5 (b). Furthermore, by increasing the PT, the LSS also increases.

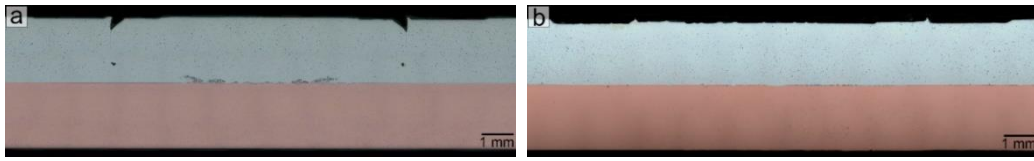


Figure 5.5 As-polished macrographs obtained with a PT of (a) 1 s and (b) 2 s. Welding condition: RS = 1200 rpm, PD = 1.6 mm, DT = 1 s, RT = 1 s.

Table 5.3 Influence of the PT on the LSS and respective fracture surface diameter. Welding condition: RS = 1200 rpm, PD = 1.6 mm, DT = 1 s, RT = 1 s.

PT (s)	LSS (kN)				Fracture surface diameter (mm)
	1	2	3	Average	
1	2.46	2.15	2.77	2.46	8.34
2	3.27	3.46	3.77	3.50	8.71

It is worth noticing that Cu or Cu-rich fragments can only be macroscopically observed along the Al/Cu interface in the welded joint obtained at a PT of 1 s. As will be further demonstrated, the peak temperature at the weld center is lower when a PT of 1 s is applied compared to a PT of 2 s. The lower heat input results in less material plasticization and as a consequence, the stirring action of the Al particles in the Cu sheet is stronger. This stirring action releases a plenty of copper fragments at the interface, which probably weakens the weld.

After achieving a defect-free weld, it was decided to maintain the RT at 1 s. Therefore, in the following experiments a PT and a RT of 2 s and 1 s, respectively, were adopted, if no specific contrary information is given.

## 5.2 Thermal Evaluation

### 5.2.1 Typical Welding Thermal Cycle

Figure 5.6 presents the results of the thermocouple assessment on the welding condition of 1200 rpm for rotational speed, 1.6 mm for plunge depth and 1 s for dwell time. The thermometry results were collected by two thermocouples embedded into the copper plate, one at the sleeve edge and other at the weld center, as presented in Figure 4.5. According to the thermal cycle features

observed in both curves, the weld process can be divided into four stages: plunging, dwelling, retraction and cooling, respectively. During the plunging, the temperature increases drastically due to the frictional heat between the tool and the material. On the second stage, the temperature keeps increasing slightly. During the sleeve retracting stage, the welding peak temperature is achieved. Finally, at the cooling stage, the temperature decreases until room temperature.

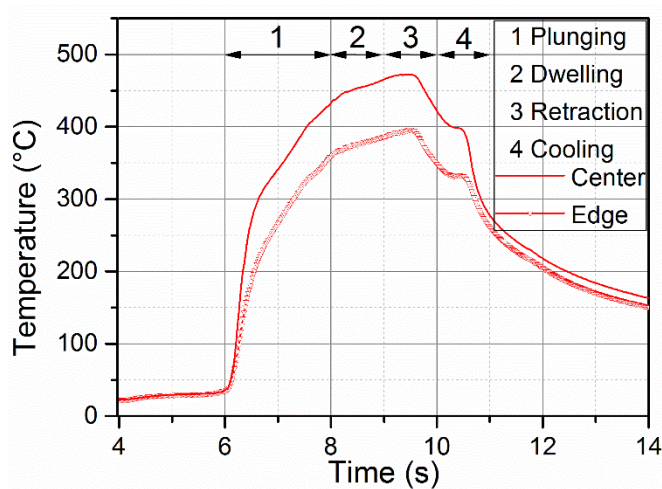


Figure 5.6 Typical thermal cycle of Al/Cu friction spot-welded joints. Welding condition: RS = 1200 rpm, PD = 1.6 mm, DT = 1 s.

For this welding condition, the highest peak temperature observed was of approximately 472°C, at the weld center. Meanwhile, the peak temperature obtained at the sleeve edge was of approximately 396°C.

### 5.2.2 Influence of Welding Parameters on Thermal Cycle

In this section, a comparison between the temperature profiles of the different levels of the parameters: plunge time; dwell time; plunge depth; and rotational speed was established. In this regard, just the temperature profile of the thermocouple positioned at the weld center was analyzed.

The comparison of the temperature profiles obtained under different PT, 1 s and 2 s, is shown in Figure 5.7. A longer PT, 2 s, results in a higher peak temperature, 44°C higher than a PT of 1 s. Moreover, when a PT of 1 s is applied,

there is a plateau during the dwelling stage, while this is not the case when the PT is 2 s.

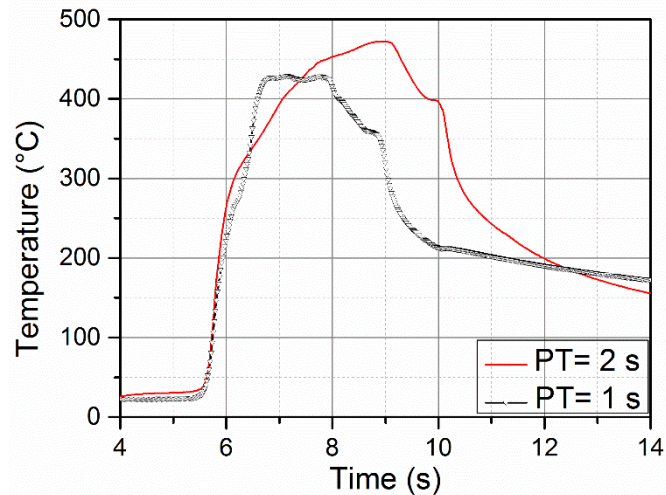


Figure 5.7 Temperature profile of comparative PT: 1 s and 2s. Welding condition: RS = 1200 rpm, PD = 1.6 mm, DT = 1 s.

Figure 5.8 shows the temperature profiles obtained at different DT, while the other parameters were kept fixed. The thermal cycles under varied DT were found to have a very similar shape. Nevertheless, by increasing the DT, the welding peak temperature slightly increases, the details of it can be found in Table 5.4.

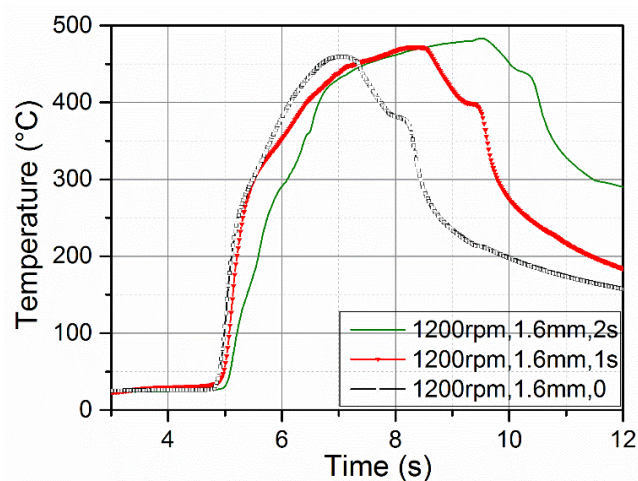


Figure 5.8 Temperature profile of comparative DT: 0, 1 s and 2 s. Welding condition: RS = 1200 rpm, PD = 1.6 mm.

Table 5.4 Influence of DT on the welding peak temperature. Welding condition:  
RS = 1200rpm, PD = 1.6 mm.

DT (s)	Peak temperature (°C)
0	459
1	472
2	483

The same conclusion can also be drawn for other welding conditions, as shown in Figure 5.9. By increasing the DT from 1 s to 2 s, at a constant rotational speed of 2000 rpm and plunge depth of 2 mm, it results in quite similar curves. Moreover, under these welding conditions, it is worth noticing that a serrated feature can be found during the dwelling stage. The same phenomenon was also observed in Al/Mg dissimilar friction spot-welded joints and it was believed to be related to alternate local melting and solidification in the weld [52]. According to Suhuddin et al. [52], the formation of the local molten material leads to a decrease in viscosity of the plasticized material; in such situation less frictional heating is generated and consequently the heating generation is affected. This probably means that the peak temperature here, close to 500°C, approaches the local melting point of the Al/Cu system, which will be later investigated.

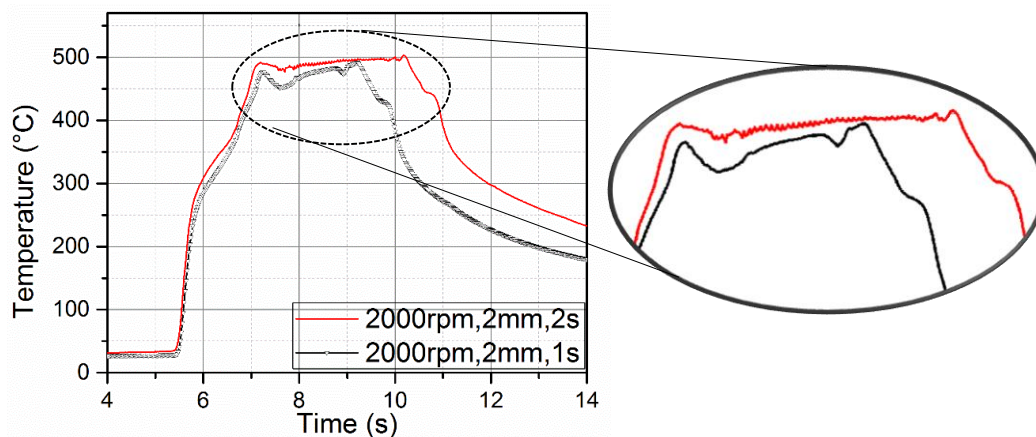


Figure 5.9 Temperature profile of comparative DT: 1 s and 2 s. The serrated feature is shown in detail. Welding condition: RS = 2000 rpm, PD = 2 mm.

The temperature profiles obtained varying only the PD parameter are shown in Figure 5.10. Considering the different levels of PD, no changes were observed

on the temperature profiles, they were found to be quite coincident. Besides, they show almost the same peak temperature, as shown in Table 5.5.

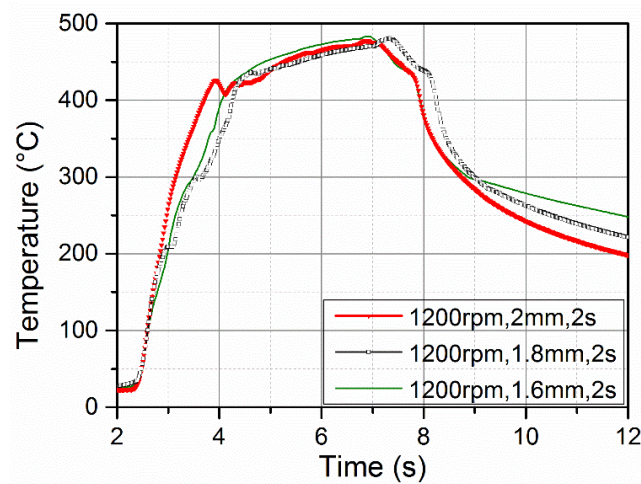


Figure 5.10 Temperature profile of comparative plunge depths: 1.6 mm, 1.8 mm and 2 mm. Welding condition: RS = 1200 rpm, DT = 2 s.

Table 5.5 Influence of PD on the welding peak temperature. Welding condition: RS = 1200 rpm, DT = 2 s.

PD (mm)	Peak temperature (°C)
1.6	483
1.8	481
2	478

Figure 5.11 shows the temperature profiles obtained at different rotational speeds, while the other parameters were kept unchanged. The RS was the parameter that proved to have the highest influence on the peak temperature. For example, the peak temperature increased from 459°C to 490°C when the tool rotational speed increased from 1200 rpm to 2000 rpm, more details can be found in Table 5.6.

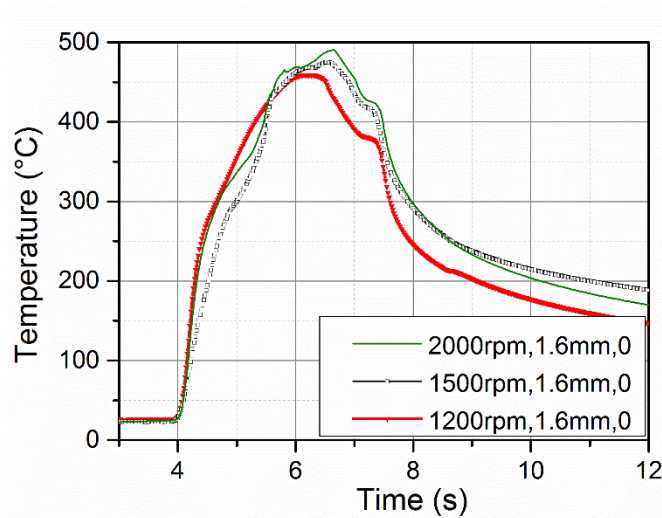


Figure 5.11 Temperature profile of comparative rotational speeds: 1200 rpm, 1500 rpm and 2000 rpm. Welding condition: PD = 1.6 mm, DT = 0.

Table 5.6 Influence of RS on the welding peak temperature. Welding condition: PD = 1.6 mm, DT = 0.

RS (rpm)	Peak temperature (°C)
1200	459
1500	475
2000	490

### 5.3 Process Parameters Optimization

#### 5.3.1 Individual Process Parameters

As previously stated, a Taguchi L9 orthogonal array, which can be used for design experiments involving three factors with three levels each, was selected to evaluate the influence of the individual process parameters on the studied responses. A L9 matrix requires only nine treatment combinations, whereas a full factorial design ( $3^3$ ) would demand 27 runs. As a Taguchi design only allows the study of a limited number of two-ways interactions, the possible existing interactions will not be considered at this stage.

The L9 orthogonal array of conditions and the corresponding LSS response from each trial is presented in Table 5.7. The objective at this stage was to



improve the response displayed in the rightmost column, assuming that larger is better.

Table 5.7 Taguchi design of experiments, the response of each run is displayed in the rightmost column.

Condition	RS (rpm)	PD (mm)	DT (s)	LSS (kN)
A1	1200	1.6	0	2.74
A2	1200	1.8	1	3.51
A3	1200	2	2	7.1
A4	1500	1.6	1	3.73
A5	1500	1.8	2	4.43
A6	1500	2	0	4.15
A7	2000	1.6	2	3.98
A8	2000	1.8	0	4.66
A9	2000	2	1	6.68

For a given process parameter combination, the variation of the LSS was found to be less than 17 %. However, significant differences were observed in the LSS value between different welding conditions, indicating that the process parameters have a strong bearing on the weld quality. Among the nine welding conditions, condition A1 and A3 showed the lowest (2.74 k N) and highest (7.1 kN) LSS, respectively.

The data distribution was verified by the normal probability plot, provided by the *Minitab* software. As illustrated in Figure 5.12, the experimental values, indicated by solid points, fall near to a straight line. This indicates that the data distribution can be considered a normal distribution, and provides the basis for additional analysis.

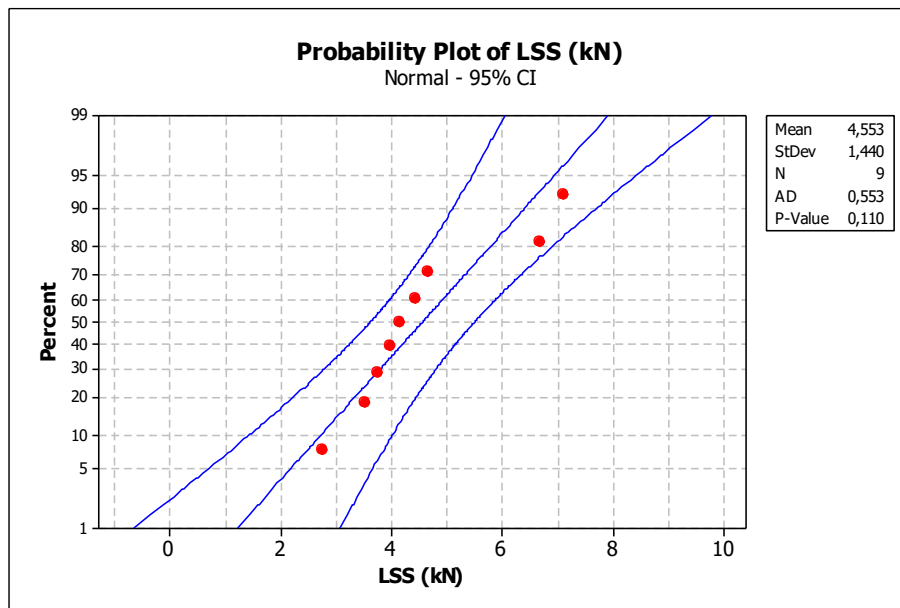


Figure 5.12 Normal probability plot.

The ANOVA of the experimental design was conducted for an  $\alpha = 0.1$  (or an interval of confidence of 90 %) and the results are shown in Table 5.8. The PD seems to have the most significant effect on the response (F ratio is higher than the critical value). On the other hand, the RS parameter appears to be statistically insignificant; this can be observed by the contribution of the RS of about 9 % in comparison to the contribution of the model error of about 15 %. However, the RS parameter could be a decisive factor in producing good welds for other welding techniques, as it was in friction stir spot welding of Al/Cu [25].

Table 5.8 Analysis of variance for the average LSS.

Source	DF	SS	V	F	P (%)
RS (rpm)	2	1558747	779374	0.63	9
PD (mm)	2	9878952	4939476	3.97	60
DT (s)	2	2654780	1327390	1.066	16
Error	2	2490179	1245090	-	15
Total	8	16582658			

Note:  $F_{\text{critical}}$  at 90% confidence = 3.11.

The response graphs, Figure 5.13, show the LSS average for each factor level. These graphs can be used to determine which level of each factor provides the best result. The level averages in Figure 5.13 show that the LSS could be

maximized when both the PD and the DT is increased, it means that the highest LSS would occur at a PD of 2 mm and DT of 2 s. As the RS was found to be statistically insignificant, it was chosen at the lower level, 1200 rpm, as it helps in minimizing the energy consumption and heat input. The parameter combination RS = 1200 rpm, PD = 2 mm and DT = 2 s was the same as the one used for condition A3, which was the one that yielded the highest LSS.

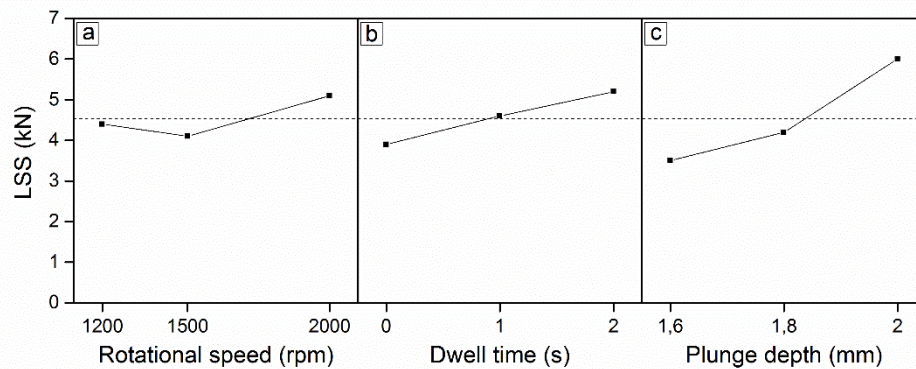


Figure 5.13 Effect of each level on the average LSS: (a) tool rotational speed, (b) dwell time and (c) plunge depth.

An OFAT experiment was conducted to confirm A3 as the optimized welding condition. The focus on this stage was improving the results achieved by the Taguchi design.

The baseline set of factor levels was the optimized welding condition determined by the Taguchi experiments (RS = 1200 rpm, PD = 2 mm and DT = 2 s). The OFAT plan studied in this work is described in Table 5.9. The LSS results of the OFAT experiments are illustrated by histograms in Figure 5.14.

Table 5.9 One-factor-at-a-time matrix of experiments.

Condition	RS (rpm)	PD (mm)	DT (s)
A3	1200	2	2
A10	1200	2	1
A11	1200	2	3
A12	1000	2	2
A13	1500	2	2
A14	1200	1.8	2
A15	1200	2.2	2

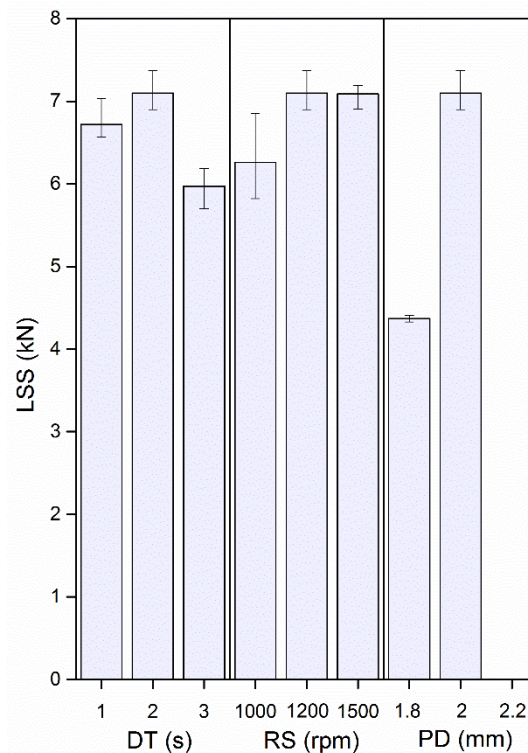


Figure 5.14 LSS response according to the OFAT plan: (a) DT variation (RS = 1200 rpm and PD = 2 mm), (b) RS variation (PD = 2 mm and DT = 2 s) and (c) PD variation (RS = 1200 rpm and DT = 2 s).

According to the OFAT plan, condition A15 should be welded. However, after some trials without success, this condition was discarded. It is believed that as the tool penetrates into the Cu sheet, Cu fragments get attached to the tool, counter acting its spin.

The results from the Taguchi and OFAT experimental designs indicate that the maximum LSS has been achieved for the welding condition: 1200 rpm for tool rotational speed, 2 mm for plunge depth and 2 s for dwell time, with an average LSS of 7.1 kN. This result was considerably higher than the minimum average load of 4.76 kN per spot that is recommended for resistance spot-welded aluminum alloys within the strength range of 240-395.9 MPa, in sheets with a thickness of 2 mm [53]. It confirms that dissimilar friction spot-welded joints of Al/Cu can yield relatively good mechanical properties.

### 5.3.2 Interactions

After analyzing all the individual process parameters in FSpW, the interactions among the factors were investigated. A useful method to visually assess interaction in the data is the interaction plot, which creates a single interaction plot for two individual factors. In these plots, the greater the deviation of the lines from the parallel state, the higher is the degree of interaction. By examining Figure 5.15, it is possible to notice the presence of interactions among factors.

As can be seen from the plot in the middle of the top row of Figure 5.15, which shows the second order interaction between PD and RS, the curves are quite parallel within PD of 1.6 and 1.8 mm, indicating no interaction. Nevertheless, PD and RS appear to interact at high value of PD. The same is occurring for the interaction between DT and RS, the interaction is observed at high level of DT, as shown in the rightmost plot of the top row of Figure 5.15. For the DT and PD interaction, presented in the middle plot of the bottom row of Figure 5.15, it is possible to notice that as the PD increases, the LSS first slightly decreases and then increases for a DT of 1 and 2 s, for a DT of 0 the opposite happens.

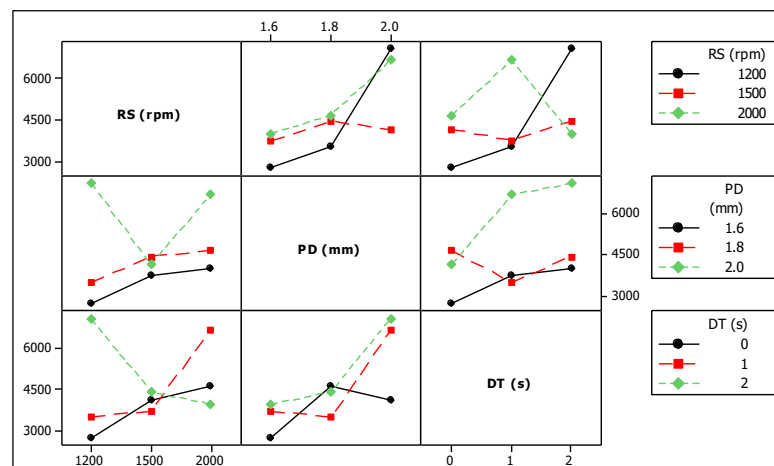


Figure 5.15 Interaction plots, obtained by the *Minitab* software.

In order to better understand the influence of the individual factors, the two-ways and three-ways interactions in the LSS, a two-level full factorial design of experiments ( $2^k$ ) was selected. In a two-level full factorial design, each

experimental factor has only two levels and the experimental runs include all combinations of these factor levels.

At this stage, a screening process was used to reduce the number of input variables by identifying the key levels controlling the interactions. The data from Figure 5.15 is not immediately clear; however, after careful examination and in an attempt to avoid a significant increase in the amount of extra runs, the levels selected to perform the full factorial design are those summarized in Table 5.10. The full factorial design and the resulting LSS for each parameter combination are presented in Table 5.11. For a given process parameter combination, variation in the LSS was found to be less than 11 %.

Table 5.10 Factors and levels for the full factorial design.

Factors	Levels	
	Level 1	Level 2
Tool rotational speed (rpm)	1200	2000
Plunge depth (mm)	1.8	2
Dwell time (s)	1	2

Table 5.11 Full factorial design of experiments used to evaluate the influence of the individual parameters and interactions, the response for each run is displayed in the rightmost column.

Condition	RS (rpm)	PD (mm)	DT (s)	LSS (kN)
A2	1200	1.8	1	3.51
A3	1200	2	2	7.1
A9	2000	2	1	6.68
A10	1200	2	1	6.72
A14	1200	1.8	2	4.37
A16	2000	1.8	1	4.59
A17	2000	1.8	2	4.99
A18	2000	2	2	5.32

To identify the possible interactions influencing the LSS, it was decided to use a Pareto plot. *Design-expert* software scales the effects in terms of standard deviations and draws a reference line on the chart, called Bonferroni Limit. Any effect that overcomes the reference line appears to be statistically significant.

The Pareto plot for the model designed at this stage is given in Figure 5.16, with the Bonferroni Limit indicated as a red dashed line. Accordingly, these results confirm the PD as the dominant factor in Al/Cu FSpW. Moreover, it suggests that the two-ways and three-ways interactions have more impact in the variation of the LSS than the individual parameters, DT and RS; however, they are not statistically significant.

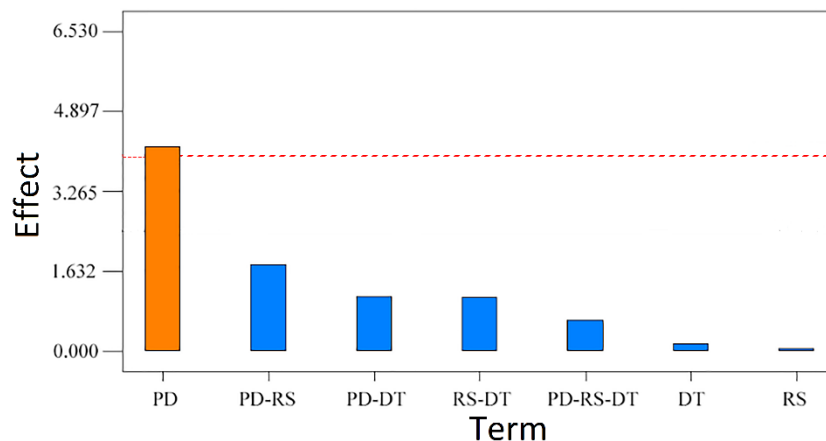


Figure 5.16 Pareto plot analysis of the individual parameters and interactions.

## 5.4 Macro and Microstructural Features

### 5.4.1 Typical Macro and Microstructural Features

Figure 5.17 (a) shows a typical macrograph view of an Al/Cu dissimilar friction spot-welded joint. An obvious border, grayish area, is formed at the SZ (hereafter it will be referred to as weld rim).

The weld rim was believed to be intermetallic compounds formed due to the interaction between the two materials. However, an image acquired from the as-polished sample at SEM in a backscatter electron mode, Figure 5.17 (b), revealed that the weld rim has no elemental contrast to the other parts of the weld or to the Al base metal (BM). Moreover, this kind of feature was also observed when two AA5083 sheets were welded in an overlap configuration, as shown in Figure 5.18.

These analyses indicate that the weld rim contrast cannot be attributed to intermetallic compounds.



Figure 5.17 Typical Al/Cu friction spot-welded joint: (a) cross section of the as-etched sample, the four white boxes indicate the region for SEM analyses in Figure 5.19; (b) back-scattered image from the as-polished sample, it was taken from the location marked with a yellow dashed box in (a). Welding condition: RS = 1200 rpm, PD = 1.6 mm, DT = 0.

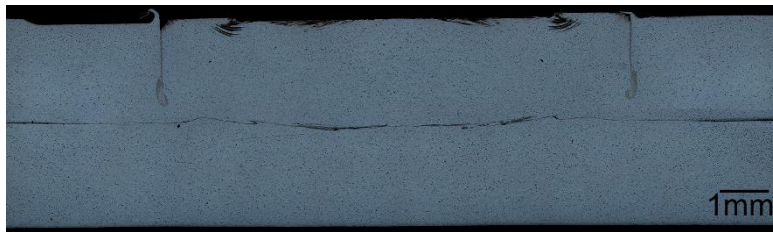


Figure 5.18 Similar AA5083 friction spot-welded joint. Welding condition: RS = 1200 rpm, PD = 1.6 mm, DT = 0.

Scanning electron microscope equipped with a concentric backscatter detector contributed to the clarification of this region, since it allows a better identification of the grain orientation contrast as well as the elemental contrast. The sample used for this analysis was first cut into small pieces by a diamond wire saw and subsequently polished by a JEOL cross section polisher. As shown in Figure 5.19 (a), the grains at the weld rim are obviously smaller than the grains of the base metal or the grains at center of the SZ, Figure 5.19 (b) and Figure 5.19 (c), respectively. These very fine and equiaxed grains are formed due to the severe plastic deformation and dynamic recrystallization that occurs during the welding process. At the Al/Cu interface, Figure 5.19 (d) and Figure 5.19 (e), some features composed of plenty of particles showing flow features can be observed. In terms of elemental contrast, these features could contain Cu or Al/Cu intermetallic. For this welding condition, the maximum depth of this flow feature into the Al sheet is about 20 µm, as indicated by the arrow in Figure 5.19 (d). It is probably impractical



only by means of atomic diffusion to transfer Cu for such a long distance, considering the peak temperature and dwell time of this welding condition. The presence of these Cu-rich particles can be attributed to the materials mixing behavior resulting from the sleeve's rotation.

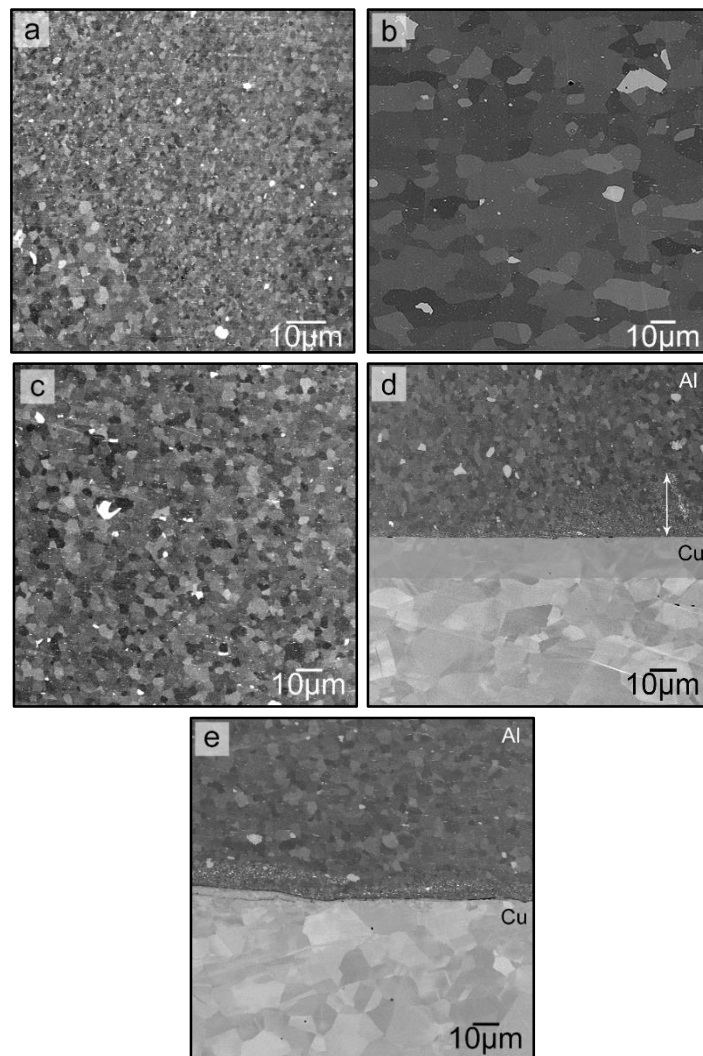


Figure 5.19 Typical microstructures of the Al/Cu welded joint: (a) weld rim, (b) BM, (c) weld center, (d) interface under the sleeve, and (e) interface at the weld center.

Further investigations suggest that under high RS and high PD, the Cu-rich particles, observed initially just close to the interface, could move further up as a result of an intense stirring and mass transport.

To facilitate the comparison between the weld rim and the Cu-rich fragments observed at the SZ, analyses were made at the welding condition 2000 rpm for

RS, 1.6 mm for PD and 0 for DT, since these regions are clearly separated from one another, as shown in Figure 5.20 (a). The grayish area, as previously mentioned, corresponds to the weld rim and the blackish area is believed to be Cu-rich particles detached from the Cu sheet. In some welding conditions, these features are overlapped, as will be shown further. The element distribution on a selected region at the blackish area is shown in Figure 5.20 (d) and Figure 5.20 (e). According to the EDS maps, the bright particles in Figure 5.20 (c) mainly consisted of Cu element.

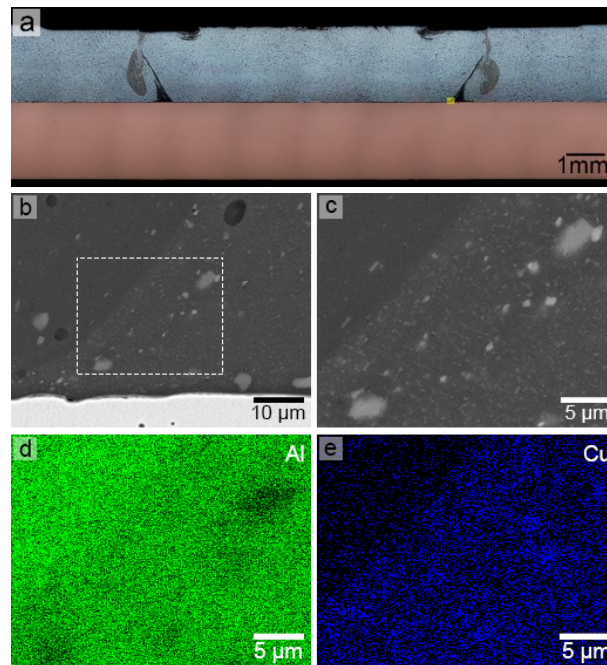


Figure 5.20 Fine particles observed at a RS of 2000 rpm, PD of 1.6 mm and DT of 0: (a) cross section of the welded joint, (b) magnified view taken from the location marked with a yellow box in (a), (c) magnified view taken from the location marked with a white box in (b), and EDS maps taken from (c): (d) Al and (e) Cu.

#### 5.4.2 Microstructure Formation Mechanism

To obtain more details of the microstructure formation mechanism, a stop-action experiment was carried out. In the stop-action experiment, the welding cycle was interrupted and forced to stop during the retraction of the sleeve. The Figure 5.21 (a) shows an overview of the welded joint obtained through this

experiment, the welding condition was 1200 rpm for RS, 2.2 mm for PD and 2 s for DT. This condition was chosen since the stirring was higher; therefore, it enables not only the visualization of a fascinating solid-state flow phenomena, but also a complex inter-diffusion and interaction between the two materials. All the micrographs in Figure 5.21 were taken in SEM at back-scattered electron mode.

Figure 5.21 (b) shows an overview of the sleeve-plunge area morphology. Stirring action can clearly be observed at the sleeve bottom. Higher magnifications of this area are shown in the Figure 5.21 (c) and Figure 5.21 (d). These swirl and vortex-like mechanisms lead to the dispersion of fine Cu fragments in the Al sheet, as shown in Figure 5.21 (e), more details are shown in Figure 5.21 (f). These scattered fragments with irregular shapes and different sizes produce a composite-like structure, which could increase the mechanical properties of the welded joint by dispersion strengthening mechanism.

As can be seen in Figure 5.21 (g), an intermetallic layer is formed around each fragment of Cu in the Al matrix. Figure 5.21 (h) shows diffusion features, which indicate that the formation of these layers is related to the mechanical effect of the sleeve, as it initiates the mass transport of Cu, and to the local diffusion induced by the temperature and enhanced by plastic deformation. In some cases, the Cu particles were totally consumed by diffusion into the surrounding Al matrix, remaining just the intermetallic layers in the matrix, as shown in Figure 5.21 (i), which is a more detailed image of the Figure 5.21 (d).

At the weld center, the Al/Cu interface can easily be identified as shown in Figure 5.22 (a). High magnification of the interface indicates the presence of two continuous, thin and uniform intermetallic layers, L1 and L2. These two layers contain some Cu and Al, but in different ratios; thus, they might be attributed to two different intermetallic compounds. In welding conditions that underwent lower heat input and lower mixing between both materials, two non-continuous layers were also observed under high magnification at the weld center, Figure 5.22 (b). The low mixing observed between the two materials in the later welding condition, as reported in Section 6.4.1, suggests that the bonding between the two materials is achieved by reactive inter-diffusion.

According to Jiang et al. [54], the lowest formation energy is attributed to the intermetallic compounds  $\text{Al}_2\text{Cu}$  and  $\text{Al}_4\text{Cu}_9$ , when the atomic percentage of copper is high enough. From the published data, the diffusivity of Cu in Al is found to be greater than that of Al in Cu [1]. Therefore, it is reasonable to expect that the  $\text{Al}_2\text{Cu}$  phase will form when the Al sheet becomes saturated with Cu. The next step of the interfacial reaction would be  $\text{Cu} + \text{Al}_2\text{Cu} \rightarrow \text{Al}_4\text{Cu}_9$  [54]. This structural evolution of the intermetallic  $\text{Al}_2\text{Cu}$  into  $\text{Cu}_9\text{Al}_4$  described the intermetallic phase formation in dissimilar AA5083 and Cu-DHP friction stir welded joints, under high heat input conditions [13].

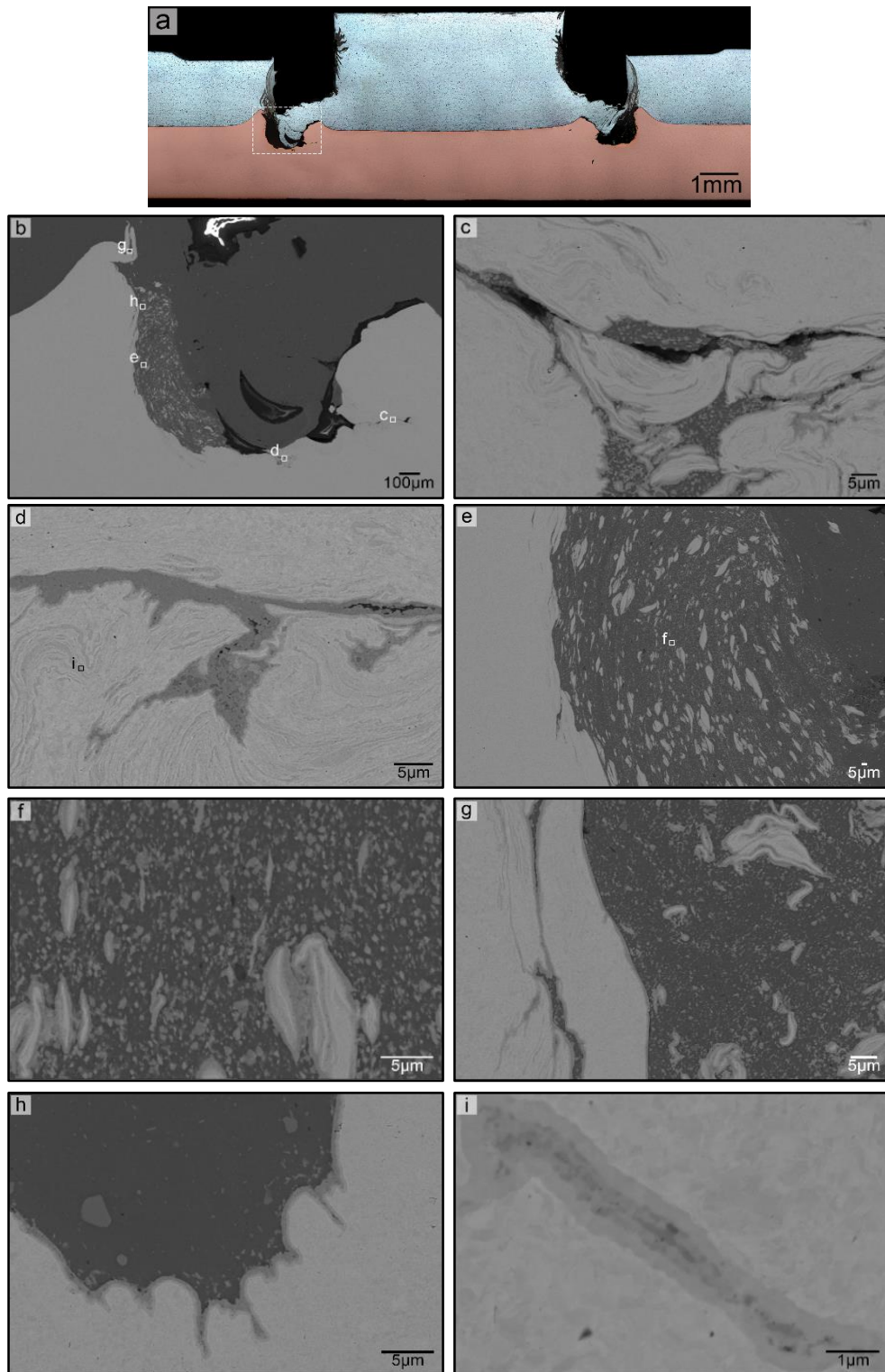


Figure 5.21 (a) Cross section of the welding condition RS = 1200 rpm, PD = 2.2 mm, DT = 2 s, the white box indicates the region for SEM analyses; (b) overview of the sleeve-plunge area, five white boxes indicate the positions of the subsequent SEM analyses; (c) and (d) swirl and vortex patterns; (e), (f) and (g) Cu fragments observed around the weld rim; (h) diffusion patterns; (i) intermetallic layers formed around each Cu fragment in the Al matrix.

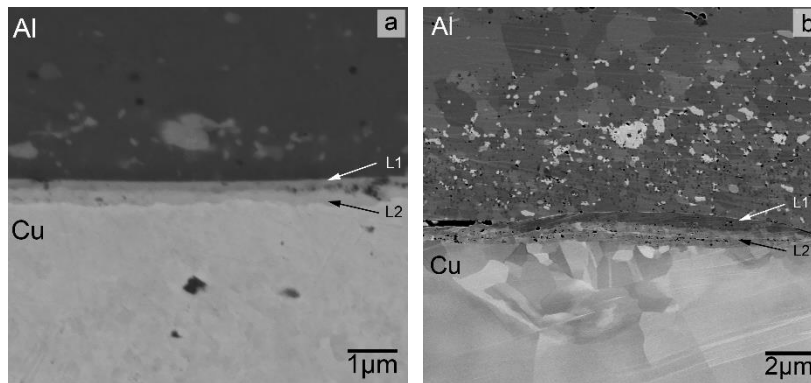


Figure 5.22 Intermetallic layers observed at the weld center: (a) welding condition: RS = 1200 rpm, PD = 2.2 mm, DT = 2 s and (b) welding condition: RS = 1200, PD = 1.6, DT = 0.

*Thermocalc* modeling software was used to determine which constituents would form, considering a hypothetical mixture of Cu to the Al substrate of 20, 25, 30, 35, 40 and 45 %, for this calculation the percentage of Mg present in the Al alloy was also proportionally considered.

The *Thermocalc* results, shown in Figure 5.23, indicate that the most likely intermetallic to form at the Al sheet is  $Al_2Cu$ . The FCC phase is aluminum solid solution, with weight compositions of Al, Cu and Mg of 97 %, 1.3 % and 1.7 %, respectively. This phase would form mainly at low values of Cu mixture. The second intermetallic phase able to form during the welding process is the S phase, which designates  $CuMgAl_2$ .

Suhuddin et al. [52] observed the formation of Al/Mg eutectic structure at approximately 450°C in Al/Mg friction spot-welded joints. This low reaction temperature shall have an important effect in this work.

The results aforementioned provide confirmatory evidence that the high percentage of Mg in the Al alloy can affect the intermetallic formation during the process.

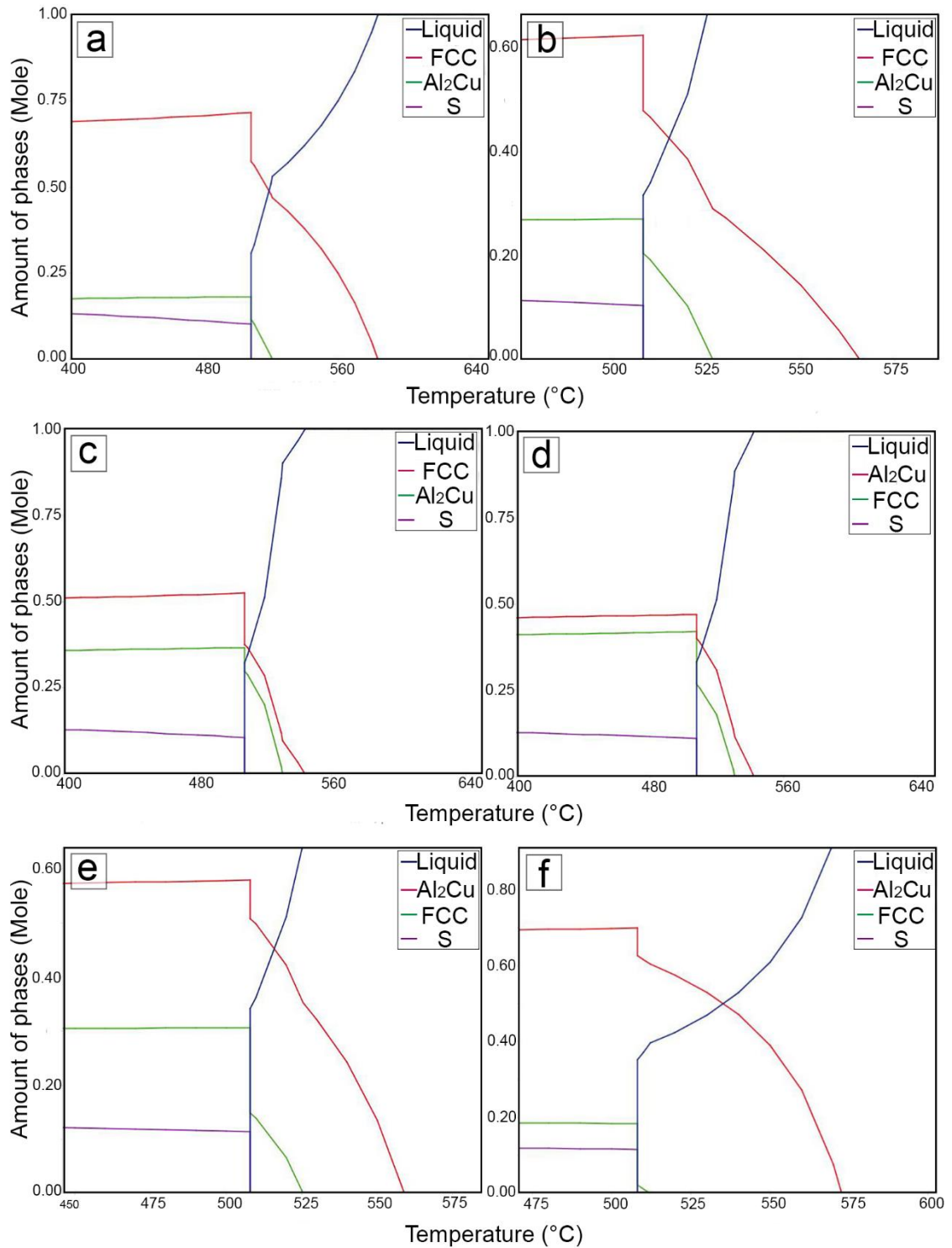


Figure 5.23 Theoretical constituents that would form considering a mixture of Cu into the Al sheet of: (a) 20, (b) 25, (c) 30, (d) 35, (e) 40 and (f) 45 (weight %).

When analyzed the center of the welding condition produced with the following parameters: RS = 2000 rpm; PD = 2 mm; and DT = 1 s, it was observed that the mechanical integration of copper into aluminum due to mass transport, plastic deformation, atomic diffusion and relatively high temperature exposure cause the formation of micro-constituents with characteristics of a eutectic structure, as shown in Figure 5.24 (b). At Figure 5.24 (c) two different eutectic micro-constituents can obviously be distinguished: a pre-eutectic phase (A) and a coupled eutectic phase, consisting of alternated layers (B).

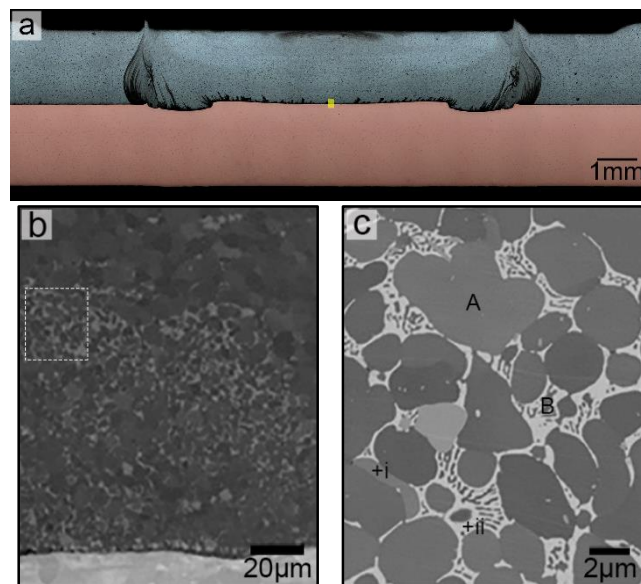


Figure 5.24 (a) Cross section; (b) region with eutectic features, taken from the location marked with a yellow box in (a); (c) details of the eutectic region, taken from the white box in (b). Welding condition: RS = 2000 rpm, PD = 2 mm, DT = 1 s.

According to the EDS maps, the matrix A contains dominant Al as well as a small amount of Cu and Mg, and thus it is primary Al. The composition variation of Cu in the primary Al grains is a result of micro-segregation. The reason for segregation is the rapid cooling imposed during the FSpW process. In such process conditions, the Cu component is expelled from the grain interior as the Al grains get supersaturated. Therefore, a diffusive feature can be seen from the Al matrix center to the grain boundary, as shown by the two arrows in Figure 5.25 (c). The dark phase of the coupled eutectic B is rich mainly in Al, while the bright phase consists of Al, Cu and Mg.



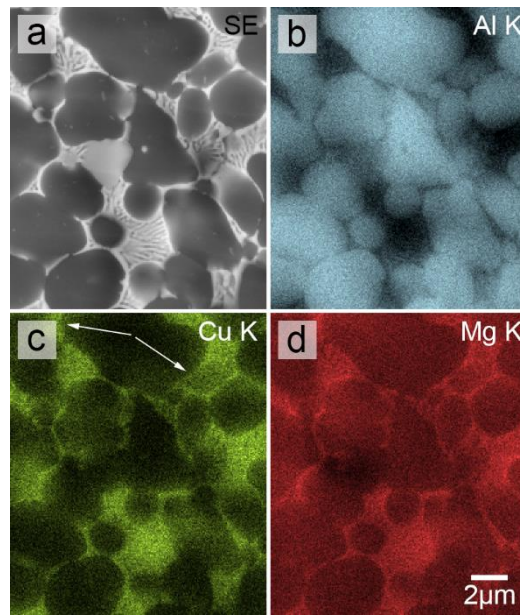


Figure 5.25 EDS maps: (a) field of view, (b) Al, (c) Cu, and (d) Mg.

The peak temperature achieved by this welding condition was of 492°C, which is significantly lower than either the Al/Cu binary eutectic reaction temperature (about 548°C) or the AA5083 solidus temperature (about 590°C). According to Effenberg et al. [26], close to the weld peak temperature, in the Al/Cu/Mg ternary-system there are two invariant reactions  $L \rightleftharpoons Al + S$  and  $L \rightleftharpoons Al + S + \theta$  (the symbols  $\theta$  and S designate  $CuAl_2$  and  $CuMgAl_2$ , respectively). Considering the quantitative result of the EDS maps around this eutectic region, the average atomic concentrations of Al, Cu and Mg are about 90%, 4% and 6%, respectively.

This composition point falls into the Al + S zone at the 400°C isothermal section of the ternary Al/Cu/Mg phase diagram, as shown by the red star in Figure 5.26. Accordingly, it indicates that only the eutectic structures free of  $\theta$  are present in the weld.

Direct quantitative EDS analyses, however, are unreliable to identify these phases, because the dimension of the eutectic structures are beyond the spatial resolution of EDS in SEM. Therefore, an integrated EDS and EBSD system, TSL Delphi package, were used to identify the phases by indexing the Kikuchi patterns based on elemental composition. The powder diffraction file data base, ICDD PDF-4+, was used for phase retrieval and identification. To improve the reliability, only grains with a confidence index (CI) higher than 0.1 and angle fit less than 1° were used for the phase identifications.

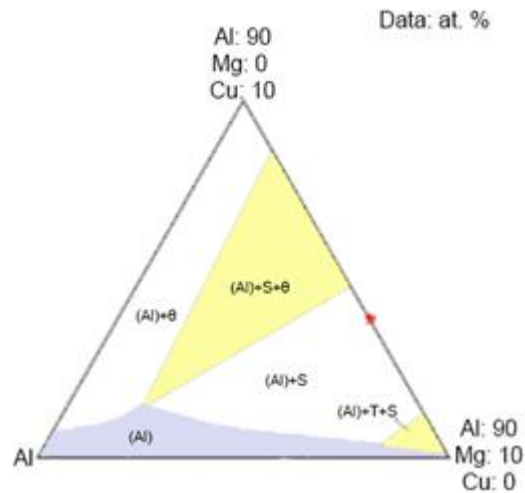


Figure 5.26 Isothermal section of ternary Al/Cu/Mg phase diagram at 400°C,  $\theta = \text{CuAl}_2$ ,  $S = \text{MgCuAl}_2$  and  $T = (\text{Cu}_{1-x}\text{Al}_x)_{49}\text{Mg}_{32}$ . The red star indicates the composition point: 90Al-4Cu-6Mg, which corresponds to the average composition of the eutectic region [55].

The results of the aforementioned analysis, which were done at the points i and ii marked in Figure 5.24 (c), are shown in Figure 5.27. It can be firstly concluded that the lattice parameters of Al, point i, are hardly influenced by the minor Cu and Mg contents, indicating that the concentrations of Cu and Mg are still within the solid solubility. Second, the bright eutectic phase in the coupled eutectic structure can be indexed as  $\text{MgCuAl}_2$ .

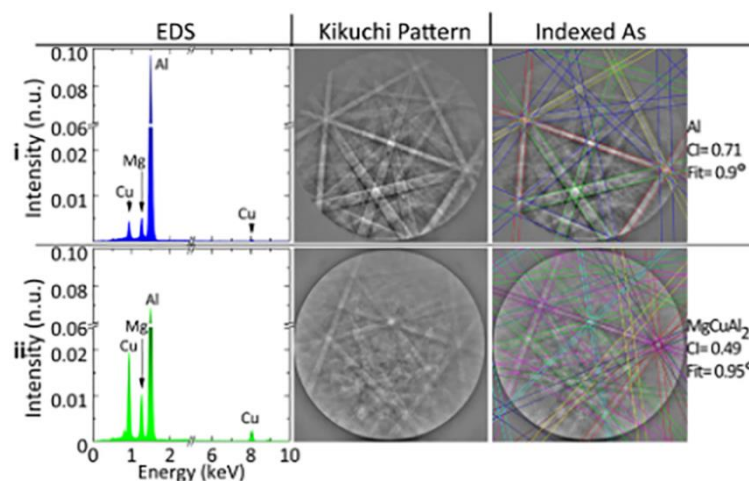


Figure 5.27 EDS spectrums and the corresponding Kikuchi patterns of points i and ii marked in Figure 5.24 (c).

Although the equilibrium calculations performed by the *Thermocalc* software in this work does not properly represent the microstructure formation mechanism for non-equilibrium conditions, such as welding processes, this technique has proven an effective and helpful method to investigate the phase evolution during the FSpW process of Al/Cu. This can be stated since the same phases identified by means of the EBSD technique were previously predicted by the theoretical calculations of the *Thermocalc* software.

The Cu supplier for the eutectic reaction should be the Cu sheet, since the BM AA5083 is nearly free of Cu. The initial mass transport of Cu results from the material flow and severe plastic deformation. The subsequent mass transport is the diffusion in solids. This phenomena is enhanced by the relatively high heat generated during the process and severe plastic deformation. A strong plastic deformation produces substantial crystal defects, such as vacancies and dislocations, that are believed to facilitate short-circuit diffusion [55].

Eutectic structures are usually undesirable because of solidification cracking tendency. In this sample, however, there is no evidence of crack formation within the weld.

## 5.5 Local Mechanical Resistance

Figure 5.28 shows a typical Vickers hardness distribution profile of an Al/Cu dissimilar friction spot-welded joint. A macrograph of the cross section is also presented in order to facilitate the visualization of the relative location of the hardness profile. The hardness in the SZ, comparing to the BM, increases due to the dynamic recrystallization induced by the thermal cycle and high strain rate imposed during the process. The higher hardness values at the weld rim are associated with the very fine recrystallized grains, and also, under high rotational speed and high plunge depth, due to the presence of Cu-rich dispersed particles around this area.

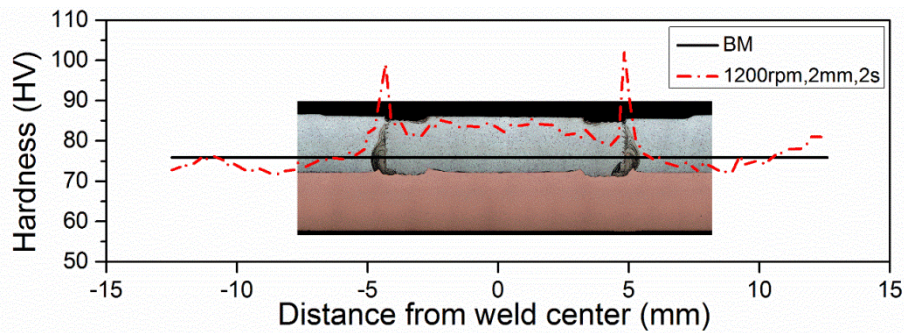


Figure 5.28 Typical hardness profile and respective cross section. Welding condition: RS = 1200 rpm, PD = 2 mm, DT = 2 s.

It is worth noticing that the microhardness profile reveals one weld zone, the SZ, apart from the BM. Other zones, TMAZ and HAZ, commonly observed in the FSpW process, do not appear evident in the case of Al/Cu dissimilar friction spot-welded joints. This is probably due to the high thermal conductivity of Cu that quickly dissipates the heat of the process.

## 5.6 Influence of Process Parameters on Macrograph and LSS

To elucidate the relation between the welding parameters and the LSS, macrographs of the different levels of each parameter: RS, PD, and DT were observed by optical microscope.

The effect of the welding parameters on the dispersion of fine Cu-rich fragments in the Al sheet, close to the weld rim, is evident when comparing the as-etched macrograph of the different levels of each parameter, as shown in Figure 5.29. The presence of Cu-rich dispersed particles creates a black contrast, just observed under a PD of 2 mm and a RS of 2000 rpm as shown in Figure 5.29 (f) and Figure 5.29 (i), respectively. In contrast, the DT does not influence this feature, because the mechanical work generated by the rotational movement of the sleeve is not enough to stir Cu fragments around the weld rim. As already mentioned, the presence of scattered fragments with irregular shapes and different sizes produces a composite-like structure, which increases the

mechanical properties of the welded joint by dispersion strengthening mechanism.

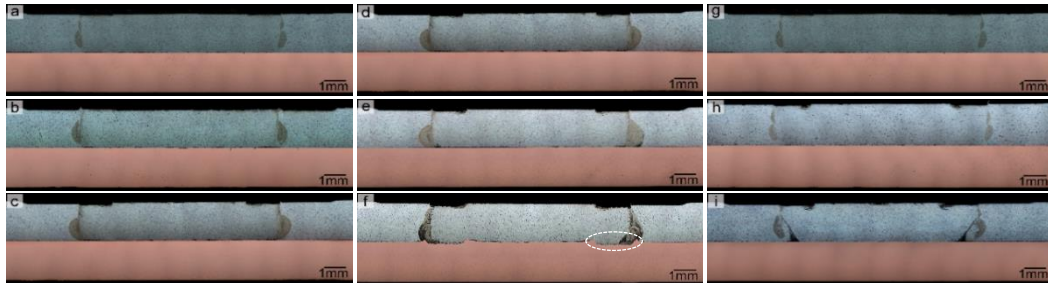


Figure 5.29 Macrograph of comparative: dwell time levels (a) 0, (b) 1 and (c) 2 s (rotational speed of 1200 rpm and plunge depth of 1.6 mm); plunge depth levels (d) 1.6, (e) 1.8 and (f) 2 mm (rotational speed of 1200 rpm and dwell time of 2 s); rotational speed levels (g) 1200, (h) 1500 and (i) 2000 rpm (plunge depth of 1.6 mm and dwell time of 0). The white dashed circle in (f) indicates the deformed metallic volume just below the interface.

To better understand the factors affecting the LSS, the bonded width was taken into account. The measured data is presented in Figure 5.30. Any significant effect can be observed when increasing the levels of the RS and PD parameters. However, it is likely that the bonded width tends to increase by increasing the DT. It could be related to the higher heat accumulation under high DT values. Increasing the bonded width leads to an increase of the load required to cause the failure, due to the fact that the effective resistance section is wider.

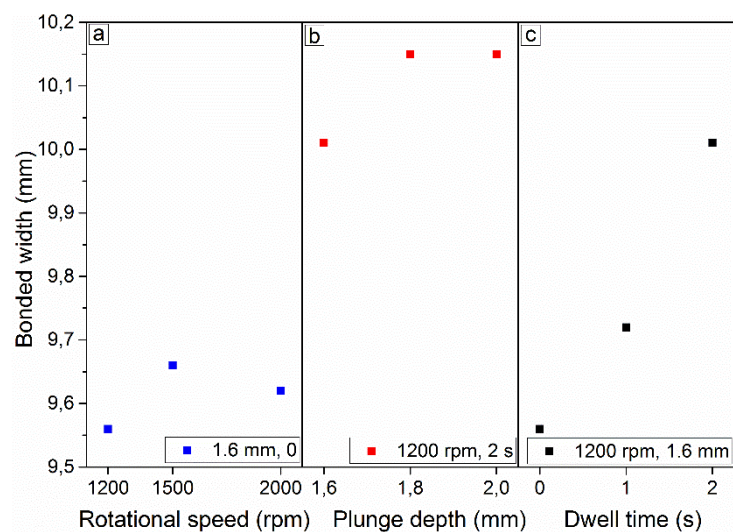


Figure 5.30 Effect of the welding parameter levels on the bonded width: (a) rotational speed, (b) plunge depth, and (c) dwell time.

The most interesting result to emerge from the comparison of the macrographs is the appearance, as the PD is increased (Figure 5.29 (f)), of a deformed metallic volume just below the interface, forming a nub inserted under the Cu sheet, which is highlighted in the image by a white dashed circle. The nub contributes to an increase of the holding forces by mechanical interlocking on the shear direction. It is likely that this feature has a significant influence over LSS, especially when the Cu vertical displacement is pronounced. Nevertheless, a PD greater than the thickness of the Al sheet, which would result in a deeper nub, could also cause difficulties to the welding process. With the increase of the RS and DT levels, no nub is observed.

The similarity in the hardness profile of the different levels of each parameter is readily observed in Figure 5.31. The only distinctive feature is the highest hardness peak for the welding condition with 1200 rpm for RS, 2 mm for PD and 2 s for DT. This is related to the presence of Cu-rich dispersed particles around the weld rim.

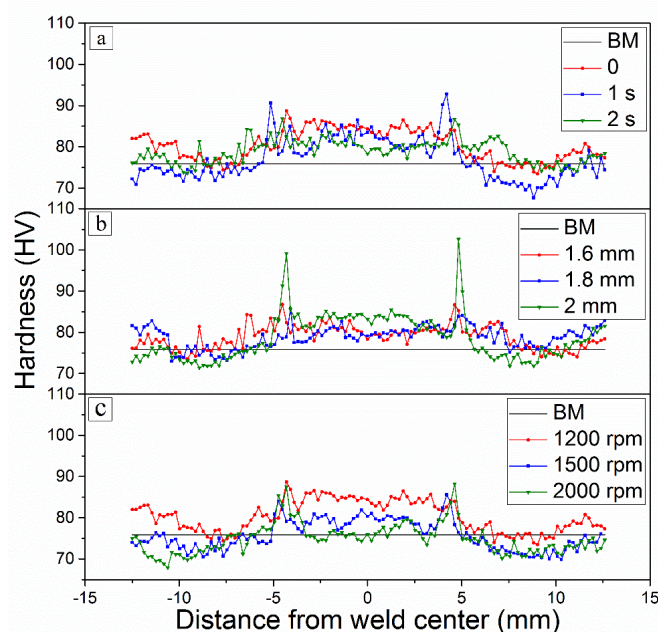


Figure 5.31 Hardness profiles comparing: (a) dwell time levels (rotational speed of 1200 rpm and plunge depth of 1.6 mm); (b) plunge depth levels (rotational speed of 1200 rpm and dwell time of 2 s); and (c) rotational speed levels (plunge depth of 1.6 mm and dwell time of 0).

## 5.7 Fracture Surface Analyses

### 5.7.1 Typical Fracture Behaviors

Scanning electron microscope was used to correlate the topography of the fracture surface to the basic mechanisms of fracture. The three typical fracture behaviors observed in this study, as well as their corresponding cross sections, are presented in Figure 5.32.

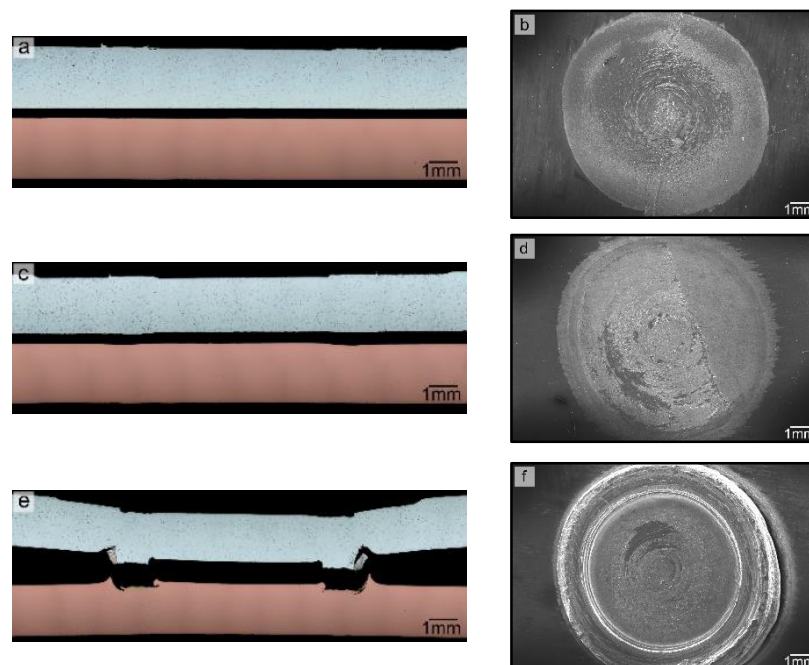


Figure 5.32 Cross section of a tested lap-shear specimen and the respective aluminum fracture surface: (a) and (b) through the interface fracture mode (weld condition: 1200 rpm, 1.6 mm, 0); (c) and (d) transitional fracture mode (weld condition: 2000 rpm, 1.8 mm, 0); (e) and (f) plug pullout with tearing (weld condition: 1500 rpm, 2 mm, 2 s).

Figure 5.32 (a) shows the mechanism described as through the interface fracture mode that happens for roughly flat samples. In this fracture behavior, the surfaces are in intimate contact but with little bonding; being, therefore, normally called as “kissing bonds”. It results in a low strength and brittle weld, in which little plastic deformation takes place prior to fracture. Moreover, the weld fails suddenly with the crack path taking place through the SZ parallel to the overlap interface.

Figure 5.32 (c) shows the cross section of the most common failure mode observed in this study. It is interesting to notice that the fracture surface shows two different regions, one with a fibrous appearance and other quite smooth, which probably indicates that the fracture propagates under both ductile and brittle mechanisms. This transitional mechanism is characterized by intermediate strength welds with a nub not considerably evident, but present.

In the plug pullout with tearing fracture mode, Figure 5.32 (e), the weld apparently failed by crossing over the nub. The mechanical interlocking between the two sheets, promoted by the nub, helps the sheets to adhere to each other during lap-shear testing. It makes the welds fractured by this mode yield a high LSS.

Figure 5.33 shows the correlation between the LSS and the fracture modes of the welds. It is possible to see that the plug pullout with tearing fracture behavior is associated with higher load carrying capacity while the interfacial failure mode is related with lower load carrying capacity.

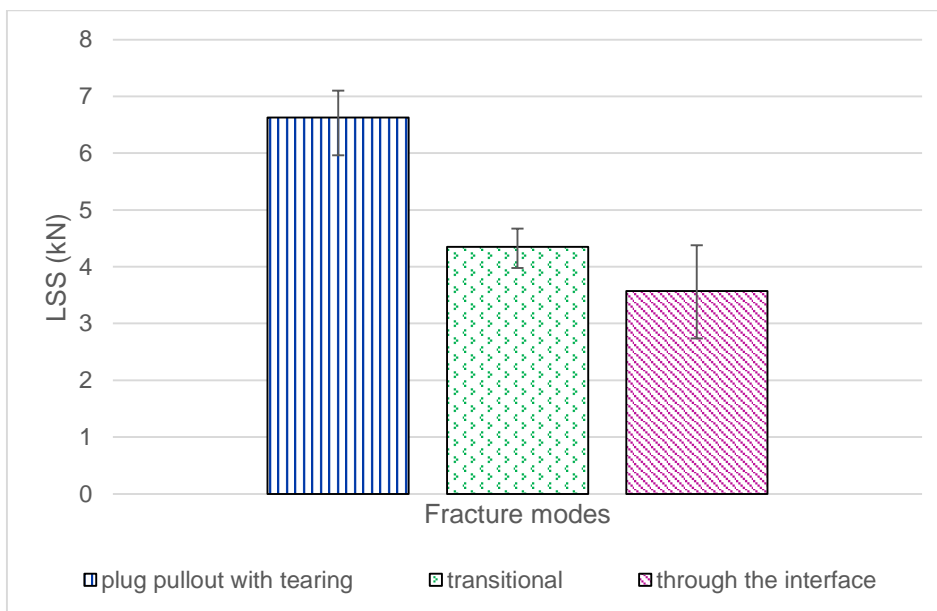


Figure 5.33 Correlation between the LSS and the fracture modes of the Al/Cu friction spot-welded joints.



### 5.7.2 Plug Pullout with Tearing

Since the plug pullout with tearing fracture mode results from sound welds, it has generally more practical interest, hence, further investigations were performed.

Figure 5.34 shows the morphology of a typical plug pullout with tearing fracture mode. In Figure 5.34, three different regions can be distinguished on both Al and Cu sheets. These regions are indicated in the Figure 5.34 (a) as regions i, ii, and iii.

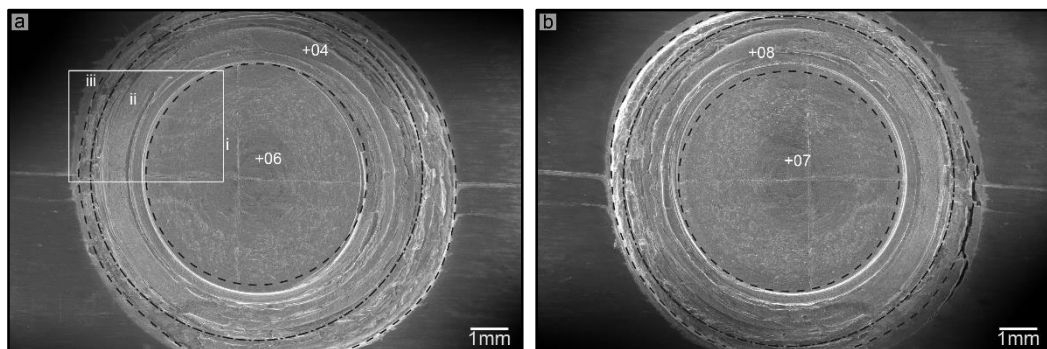


Figure 5.34 Fracture morphology of a plug pullout with tearing fracture mode: (a) Cu fracture surface and (b) Al fracture surface. The two dashed lines show the boundary of region i and region ii; the dash-dotted line shows the profile of the sleeve.

Region i has the same diameter as the tool pin (its border coincides with the pin profile). It implies that this region was not obviously subjected to shear deformation during lap-shear testing. As observed, when compared the dash-dot line, which corresponds to the outer profile of the sleeve, to the second dash line, which corresponds to the edge of region ii, the later one presents a larger diameter than the previous. It suggests that region ii suffered tearing and underwent a higher deformation. Region iii, located between the BM and region ii, shows a relatively smooth surface. These results show that among these regions, ii is the one that contributes most to the LSS.

Figure 5.35 (b) shows the details of region iii. According to the EDS results, shown in Table 5.12, location A is just copper BM. Location B, smooth in surface,

mainly contains Al and Cu, but it is predominant in Cu. And location C, rough in surface, contains similar contents of Al and Cu.

Region ii shows a quite complex morphology. During welding, due to the penetration of the sleeve and deformation, this area was formed below the original Al/Cu interface. Area 02, which is located outside the outer profile of the sleeve, shows no detectable Cu (location D). It seems that the fracture path follows locally through the Al in the weld. Probably, it is the reason for the local ductile fracture feature. Area 03, which locates at the bottom of region ii, shows a relatively smooth surface, as shown in Figure 5.35 (d). Energy dispersive spectroscopy results reveal that this area is mixed by Al and Al-rich intermetallic compounds (locations E and F).

Region i is just under the pin. Its morphology is predominant in areas such as position L, as shown in Figure 5.35 (e). The EDS results of locations K and L are presented in Table 5.12. Position L is basically Cu-rich intermetallic, while location K is Cu solid solution.

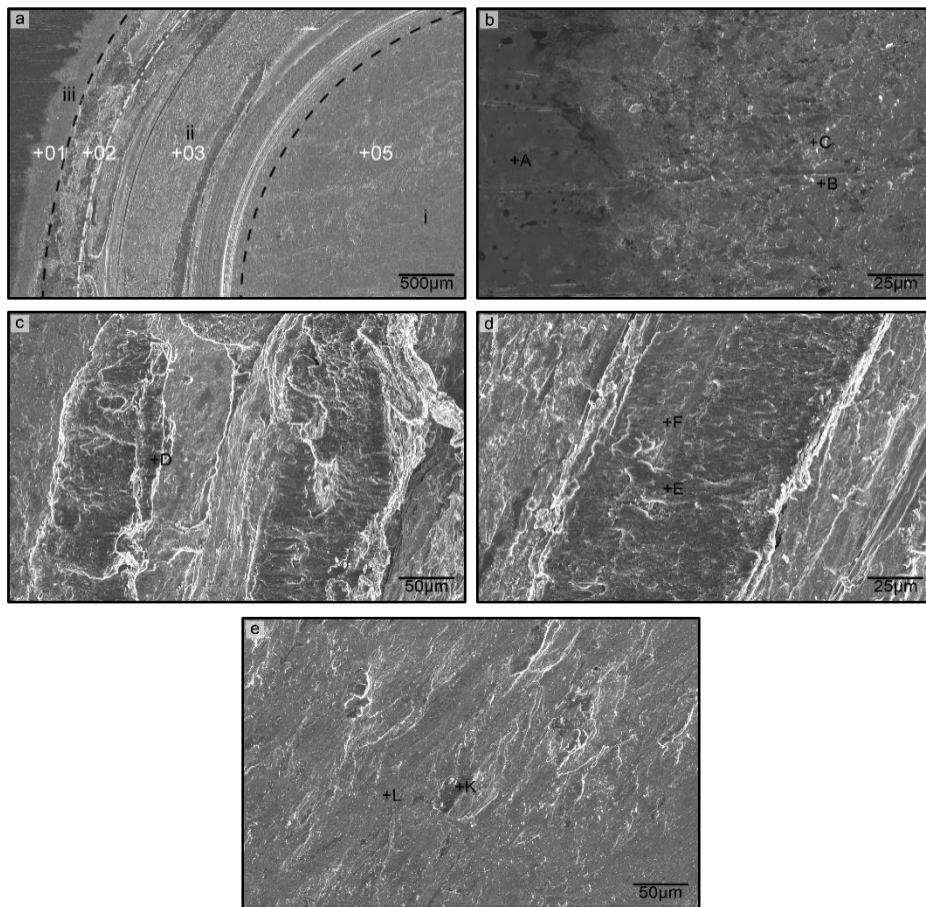


Figure 5.35 Fracture morphology of different areas: (a) an overview (marked in Figure 5.34 (a) by a white box), (b) area 01, (c) area 02, (d) area 03 and (e) area 05. Area 01, area 02 and area 03, and area 05 locate at regions i, ii, and iii, respectively.

Table 5.12 Elemental composition of different locations in Figure 5.35 (atomic %).

Location	Region	Mg	Al	Cu	Comments
A	Cu BM	-	-	100	Cu base metal
B	iii	1.5	27.7	70.8	Cu-rich intermetallic
C	iii	7.6	50.0	42.4	Al-rich intermetallic
D	ii	5.8	92.7	1.5	Al solid solution
E	ii	4.75	91.94	3.31	Al solid solution
F	ii	4.75	61.63	33.62	Al-rich intermetallic
K	i	-	4.46	95.54	Cu(Al) solid solution
L	i	3.18	32.44	64.38	Cu-rich intermetallic

Figure 5.36 shows the fracture features of region ii on the same area of both Cu and Al sheets, position 04 and 08 marked in Figure 5.34 (a) and Figure 5.34 (b), respectively. For the same location on the two sheets, where they were welded before lap-shear testing, the elemental compositions are different. For example, the location I on the Al side is basically Al solid solution, while the same location on Cu side, location G, contains slightly more Al than Cu. Also, the location J on Al side is rich in Al, while the location H contains much more Cu. This indicates that the fracture paths follow the interface between two different phases.

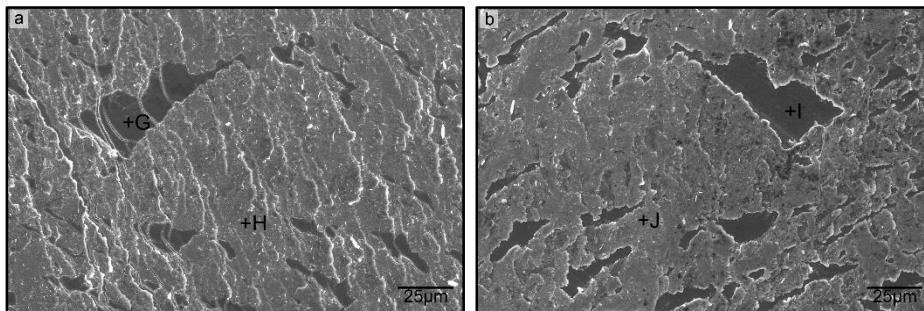


Figure 5.36 Fracture surface correlation of the same area on both sheets at region ii: (a) Cu sheet and (b) Al sheet.

Table 5.13 Elemental composition of different locations in Figure 5.36 (atomic %).

Location	Region	Mg	Al	Cu	Comments
G	ii (Cu side)	4.26	53.23	42.51	Al-rich intermetallic
H	ii (Cu side)	-	31.28	68.72	Cu-rich intermetallic
I	ii (Al side)	3.14	94.12	2.29	Al solid solution
J	ii (Al side)	4.56	76.23	18.01	Al-rich intermetallic

The same was done for the area around the weld center, region i, which shows a smoother fracture morphology. The details of such an area on the Cu sheet, position 06 marked in Figure 5.34 (a), are shown in Figure 5.37 (a). Meanwhile the same area on the Al sheet, position 07 marked in Figure 5.34 (b), is presented in Figure 5.37 (b). According to the EDS results, shown in Table 5.14, the same conclusion can be drawn. The fracture paths follow the interfaces between two

different phases: Al / Al-rich intermetallic and Al-rich intermetallic / Cu-rich intermetallic.

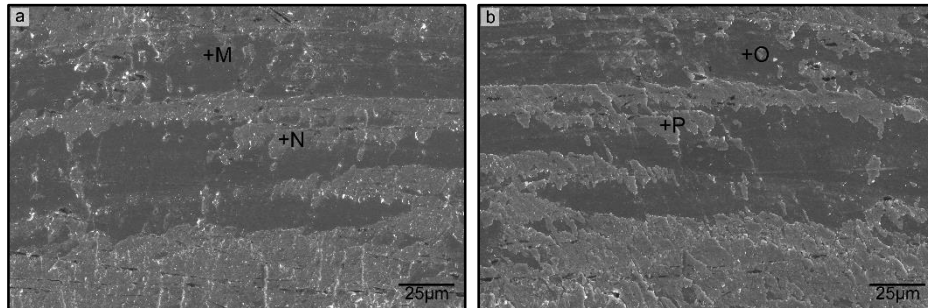


Figure 5.37 Fracture surface correlation of the same area on both sheets at region i: (a) Cu sheet and (b) Al sheet.

Table 5.14 Elemental composition of different locations in Figure 5.37 (atomic %).

Location	Region	Mg	Al	Cu	Comments
M	i (Cu side)	8.59	37.10	54.30	Al-rich intermetallic (The discrepancy in Cu is due to the matrix)
N	i (Cu side)	-	27.74	72.26	Cu-rich intermetallic
O	i (Al side)	5.84	88.55	3.07	Al solid solution
P	i (Al side)	7.43	81.25	8.62	Al-rich intermetallic

Considering the quantitative results of the EDS, the average atomic concentrations of the Cu-rich intermetallic and the Al-rich intermetallic are: Cu = 69.0 %, Al = 29.8 %, Mg = 1.17 %; and Cu = 29.0 %, Al = 64.5 %, Mg = 5.7 %, respectively. According to the Al/Cu equilibrium phase diagram, presented in Figure 3.2, these compositions are attributed to the intermetallic compounds  $\text{Al}_4\text{Cu}_9$  and  $\text{Al}_2\text{Cu}$ .

Since smooth areas imply weak bonding, it is deducible, from the morphology shown in Figures 6.36 and 6.37, that the interface between the Al and the  $\text{Al}_2\text{Cu}$  intermetallic is not as strong as that between the  $\text{Al}_2\text{Cu}$  intermetallic and the  $\text{Al}_4\text{Cu}_9$  intermetallic.

Since the smoother areas in region i are more extensive than those of region ii, it is suggested that a better weld strength of Al to Cu is achieved in region ii.

Also it is noteworthy that the smooth area occurs more frequently in the center of region i rather than in the surrounding. It means that the surrounding possesses higher bonding strength than the weld center, which can also be found by the residual feature of scratches on Figure 5.34.

## 6 CONCLUSIONS

From the results obtained in this work, the following considerations can be established:

(1) The combination of two optimization techniques, taguchi and one-factor-at-a-time, revealed an easy and simple procedure for determining the optimized welding condition. The results suggest that a rotational speed of 1200 rpm, plunge depth of 2 mm and a dwell time of 2 s would improve the lap-shear strength. The Pareto plot generated by a  $2^3$  - full factorial design indicated that the second and third order interactions are not statistically significant.

(2) At the stir zone a grayish area was observed, namely weld rim. This contrast results from the presence of very fine and equiaxed grains, formed due to severe plastic deformation and dynamic recrystallization. Under high rotational speed and high plunge depth, Cu-rich particles could move towards the upper part of the Al sheet as a result of mass transport. The microstructural analyses and microhardness profiles revealed one distinct weld area, the stir zone. The higher hardness values were detected at the weld rim, mainly as a result of the more refined microstructure and occasionally, due to the presence of Cu-rich particles. Two layered intermetallic structures were observed at the center of welding conditions that underwent high and low heat inputs during the process. The reactive inter-diffusion that forms these layers is responsible for the bonding between the two materials. According to theoretical calculations performed by the *Thermocalc* software, the most likely phases to form during the process are  $Al_2Cu$ , Al solid solution and  $CuMgAl_2$ . Due to the combination of mass transport, plastic deformation, atomic diffusion, relatively high temperature exposure and the special alloy system of base metal AA5083, some welding conditions underwent an eutectic reaction, forming an  $CuMgAl_2$  eutectic structure.

(3) The presence of a deformed metallic volume just below the interface (nub) has a significant influence over the weld strength, especially when the Cu vertical displacement was significant. It was also concluded that the sleeve plunge depth plays an important role in the nub displacement feature.

(4) Lap-shear testing specimens investigated in this work presented three types of fracture mechanisms: through the interface, plug pullout with tearing and a transitional one. In case of the plug pullout failure, the fracture paths followed the interface between the two different phases, Al / Al<sub>2</sub>Cu and Al<sub>2</sub>Cu / Al<sub>4</sub>Cu<sub>9</sub>, being the last path stronger than the previous one.



## 7 RECOMMENDATIONS FOR FUTURE WORK

The recommendations for future work are summarized below:

- (1) Investigate the friction spot weldability of Al and Cu, considering as base metal an aluminium alloy that is commonly applied in the HVAC segment, such as: AA6201, AA6101, AA1120, AA1350.
- (2) A study of the electrical properties of the Al/Cu friction spot-welded joints would provide further information about the weld quality, since the greatest use of these welds requires high electrical conductivity.
- (3) Investigate the effects of a long-term service life on the weld quality. Thermal effects are clearly of considerable significance considering intermetallic growth and could, with benefit, be studied in friction spot-welded joints of Al/Cu.



## 8 REFERENCES

- [1] J. P. Bergmann, F. Petzoldt, R. Schürer, and S. Schneider, "Solid-state welding of aluminum to copper—case studies," *Weld World*, vol. 57, no. 4, pp. 541–550, Apr. 2013.
- [2] H. J. Liu, J. J. Shen, L. Zhou, Y. Q. Zhao, C. Liu, and L. Y. Kuang, "Microstructural characterisation and mechanical properties of friction stir welded joints of aluminium alloy to copper," *Science and Technology of Welding and Joining*, vol. 16, no. 1, pp. 92–98, Jan. 2011.
- [3] M. Marya and S. Marya, "Interfacial microstructures and temperatures in aluminium–copper electromagnetic pulse welds," *Science and Technology of Welding and Joining*, vol. 9, no. 6, pp. 541–547, Dec. 2004.
- [4] S. T. Amancio-Filho, A. P. C. Camillo, L. Bergmann, J. F. dos Santos, S. E. Kury, and N. G. A. Machado, "Preliminary Investigation of the Microstructure and Mechanical Behaviour of 2024 Aluminium Alloy Friction Spot Welds," *Mater. Trans.*, vol. 52, no. 5, pp. 985–991, May 2011.
- [5] U. Suhuddin, L. Campanelli, M. Bissolatti, H. Wang, R. Verastegui, and J. F. dos Santos, "A review on microstructural and mechanical properties of friction spot welds in Al-based similar and dissimilar joints," in *Proceedings of the 1st International Joint Symposium on Joining and Welding*, H. Fujii, Ed. Woodhead Publishing, pp. 15–21, 2013.
- [6] Handbook of *Properties and Selection: Nonferrous Alloys and Special-Purpose Materials*, 10th ed. USA: ASM International, 1990.
- [7] London Metal Exchange. Available from <http://lme.com/> [Accessed 14 September 2015].

[8] M. F. Ashby, "Case studies—multiple constraints and conflicting objectives," in *Materials Selection in Mechanical Design*, 3rd ed. Oxford: Elsevier, pp. 279, 2005.

[9] J. L. Campbell, "Welding Aluminum Different, but not Difficult," *Fabricator*, pp. 1-4, May-June 1999.

[10] J. E. Hatch, *Aluminum: Properties and Physical Metallurgy*. - ASM International, pp.26-27, 1984

[11] S. Amancio, PhD-thesis: "Friction Riveting: development and analysis of a new joining technique for polymer-metal multi-materials structures," Technischen Universität Hamburg-Harburg (TUHH), 2007.

[12] TWI-global. Available from <http://www.twi-global.com/technical-knowledge/job-knowledge/weldability-of-materials-aluminium-alloys-021/> [Accessed 15 October 2016].

[13] I. Galvão, J.C. Oliveira, A. Loureiro, and D. M. Rodrigues, "Formation and distribution of brittle structures in friction stir welding of aluminum and copper: influence of process parameters," *Science and Technology of Welding and Joining*, vol. 16, no. 8, 2011.

[14] H. J. Liu, J. J. Shen, L. Zhou, Y. Q. Zhao, C. Liu, and L. Y. Kuang, "Microstructural characterization and mechanical properties of friction stir welded joints of aluminum alloy to copper," *Science and Technology of Welding and Joining*, vol. 16, no. 1, 2011.

[15] MatWeb: Online Materials Information Resource. Available from <http://www.matweb.com/> [Accessed 14 September 2015].

- [16] W. D. Callister, "Propriedades Elétricas," in *Ciência e Engenharia de Materiais uma introdução*, 7th ed. Rio de Janeiro: LTC, pp. 495-497, 2008.
- [17] Handbook of *Welding Copper and Copper Alloys*, 8th ed. Miami: American Welding Society, 1997.
- [18] T. G. Nieh and W. D. Nix, "Embrittlement of copper due to segregation of oxygen to grain boundaries," *MTA*, vol. 12, no. 5, pp. 893–901, May 1981.
- [19] KME Italy S.p.A.: "Copper Strips, Copper Sheets, Copper Discs material data sheet," Cu-DHP, Fornaci di Barga, Italy, 2013.
- [20] C. Genevois, M. Girard, B. Huneau, X. Sauvage, and G. Racineux, "Interfacial Reaction during Friction Stir Welding of Al and Cu," *Metallurgical and Materials Transactions*, vol. 42A, pp. 2290-2295, 2011.
- [21] J. L. Murray, "The aluminium-copper system," *International Metals Reviews*, vol. 30, no. 1, pp. 211–234, Jan. 1985.
- [22] N. Ponweiser, C. L. Lengauer, and K. W. Richter, "Re-investigation of phase equilibria in the system Al–Cu and structural analysis of the high-temperature phase  $\eta_1$ -Al<sub>1</sub>- $\delta$ Cu," *Intermetallics*, vol. 19, no. 11, pp. 1737–1746, Nov. 2011.
- [23] D. M. Rabkin, V. R. Ryabov, A. V. Lozovskaya, and V. A. Dovzhenko, "Preparation and properties of copper-aluminum intermetallic compounds," *Powder Metall Met Ceram*, vol. 9, no. 8, pp. 695–700, Aug. 1970.
- [24] E. R. Wallach and G. J. Davies, "Mechanical properties of aluminium-copper solid-phase welds," *Metals Technology*, vol. 4, no. 1, pp. 183–190, Jan. 1977.

[25] R. Heideman, C. Johnson, and S. Kou, "Metallurgical analysis of Al/Cu friction stir spot welding," *Science and Technology of Welding and Joining*, vol. 15, no. 7, pp. 597–604, Oct. 2010.

[26] G. Effenberg and A. Prince, updated by N. Lebrun, H. L. Lukas, and M. G. Harmelin, "Al-Cu-Mg (Aluminium - Copper - Magnesium)," in *Light Metal Systems, Part 2*, edited by G. Effenberg and S. Ilyenko. Berlin/Heidelberg: Springer, 2005.

[27] C. Schilling and J. F. dos Santos, "Method and device for linking at least two adjoining work pieces by friction welding," European patent EP 1230062 B1 (WO 2001/036144), 17 May 2006.

[28] S. T. Amancio-Filho, C. Bueno, J. F. dos Santos, N. Huber, and E. Hage Jr., "On the feasibility of friction spot joining in magnesium/fiber-reinforced polymer composite hybrid structures," *Materials Science and Engineering: A*, vol. 528, no. 10–11, pp. 3841–3848, Apr. 2011.

[29] D. Mitlin, V. Radmilovic, T. Pan, J. Chen, Z. Feng, and M. L. Santella, "Structure–properties relations in spot friction welded (also known as friction stir spot welded) 6111 aluminum," *Materials Science and Engineering: A*, vol. 441, no. 1–2, pp. 79–96, Dec. 2006.

[30] C. Oberembt, C. D. Allen, W. J. Arbegast, A. Patnaik, "Screening for process variable sensitivity in refill friction spot welding of 6061 aluminum sheet". In: Mishra RS, Mahoney MW, Lienert TJ, Jata KV, editors. 136th annual meeting and exhibition TMS2009 – friction stir welding and processing IV, Orlando, USA, February 25<sup>th</sup> – March 1st 2007. The Minerals, Metals and Materials Society – TMS, 2007.

- [31] S. Lathabai, M. J. Painter, G. M. D. Cantin, V. K. Tyagi, "Friction Stir Spot Welding of Automotive Lightweight Alloys," in *Proceedings of the 7th International Conference*. ASM International, pp. 207-212, 2006.
- [32] A. Echeverria, A. Zabaleta, P. Alvarez, E. Aldanondo, J. Solis, A.A.M. da Silva, "Influence of Welding Parameters and Tool Geometry on the Mechanical Performance of Friction Stir Spot Welded Al-Mg alloys," *Trends in Welding Research: Proceedings of the 8th International Conference*, June 1-6, 2008, Callaway Gardens Resort, Pine Mountain, Georgia, USA. ASM International, 2009.
- [33] P. Su, A. Gerlich, T.H. North, G. J. Bendzsak, "Energy generation and stir zone dimensions in friction stir spot weldings," *SAE technical series*, 2006.
- [34] P. Su, A. Gerlich, T. H. North, and G. J. Bendzsak, "Energy utilisation and generation during friction stir spot welding," *Science and Technology of Welding and Joining*, vol. 11, no. 2, pp. 163–169, Mar. 2006.
- [35] P. Su, A. Gerlich, T. H. North "Friction Stir Spot Welding of Aluminum and Magnesium Alloy sheets," *SAE technical paper*, 2005.
- [36] W. S. Chang, H. J. Cho, H. J. Kim, and C. K. Chun, "Evaluation of Friction Spot Joining Weldability of Al Alloys for Automotive," *Materials Science Forum*, vol. 539–543, pp. 411–416, 2007.
- [37] S. Bozzi, A. L. Etter, T. Baudin, A. Robineau, and J. C. Goussain, "Mechanical Behaviour and Microstructure of Aluminum-Steel Sheets Joined by FSSW," *Texture, Stress, and Microstructure*, 2008.
- [38] G. F. P. Cipriano, Master-thesis: "New Assembly Concepts and Technology for Metallic Structures of Next Generation Fuselage," Instituto Superior Técnico, 2014.

- [39] T. Rosendo, B. Parra, M. A. D. Tier, A. A. M. da Silva, J. F. dos Santos, T. R. Strohaecker, and N. G. Alcântara, "Mechanical and microstructural investigation of friction spot welded AA6181-T4 aluminium alloy," *Materials & Design*, vol. 32, no. 3, pp. 1094–1100, Mar. 2011.
- [40] R.S. Mishra, Z.Y. Ma, "Friction Stir Welding and Processing," *Materials Science and Engineering*, pp. 1-78, 2005.
- [41] T. S. Rosendo, PhD-thesis: "Estudo do Desempenho Mecânico de Solda(s) Ponto por Fricção (FSpW) da Liga AA6181-T4," Universidade Federal do Rio Grande do Sul (UFRGS), 2009.
- [42] P. Su, A. Gerlich, T. H. North, and G. J. Bendzsak, "Intermixing in dissimilar friction stir spot welds," *Metall. Mater. Trans. A-Phys. Metall. Mater. Sci.*, vol. 38A, no. 3, pp. 584–595, Mar. 2007.
- [43] D. Montgomery, "The Taguchi Approach to the Design of Experiments," in *Design and Analysis of Experiment*, 3rd ed. New Jersey: John Wiley & Sons, pp. 370-399, 1991.
- [44] M. Yousefieh, M. Shamanian, and A. Saatchi, "Optimization of the pulsed current gas tungsten arc welding (PCGTAW) parameters for corrosion resistance of super duplex stainless steel (UNS S32760) welds using the Taguchi method," *Journal of Alloys and Compounds*, vol. 509, no. 3, pp. 782–788, Jan. 2011.
- [45] D. D. Frey, F. Engelhardt and E. M. Greitzer, "A role for "one-factor-at-a-time" experimentation in parameter design," *Research in Engineering Design*, vol. 14, pp. 65-74, 2013.
- [46] L. C. Campanelli: "Estudo do Processo de Soldagem por Fricção por Ponto da Liga de Magnésio AZ31," Universidade Federal de São Carlos (UFSCar), 2012.



[47] Uddeholm: "Uddeholm Hotvar product data sheet," 2011.

[48] INTERNATIONAL ORGANIZATION FOR STANDARDIZATION. Standard *ISO 14273*: "Specimen dimensions and procedure for shear testing resistance spot, seam and embossed projection welds," 2000.

[49] American Society for Testing and Materials. Standard *ASTM E384-11*: "Standard Test Method for Knoop and Vickers Hardness of Materials Specimen," 2011.

[50] American Welding Society. Standard *AWS D17.2*: "Specification for Resistance Welding for Aerospace Applications," 2013.

[51] C.W. Tan, Z.G. Jiang, L.Q. Li, Y.B. Chen, X.Y. Chen, "Microstructural evolution and mechanical properties of dissimilar Al-Cu joints produced by friction stir welding," *Materials & design*, vol. 51, pp. 466–473, 2013.

[52] U. F. H. Suhuddin, V. Fischer, and J. F. dos Santos, "The thermal cycle during the dissimilar friction spot welding of aluminum and magnesium alloy," *Scripta Materialia*, vol. 68, no. 1, pp. 87–90, Jan. 2013.

[53] Welding, Resistance: Spot and Seam, SAE Standard *AMS-W-6858A*, SAE International, 2005.

[54] H. G. Jiang, J. Y. Dai, H. Y. Tong, B. Z. Ding, Q. H. Song, and Z. Q. Hu, "Interfacial reactions on annealing Cu/Al multilayer thin films," *Journal of Applied Physics*, vol. 74, no. 10, pp. 6165–6169, Nov. 1993.

[55] J. Shen, U. F. H. Suhuddin, M. E. B. Cardillo, and J. F. dos Santos, "Eutectic structures in friction spot welding joint of aluminum alloy to copper," *Applied Physics Letters*, vol. 104, no. 19, May 2014.